Alma Mater Studiorum · University of Bologna

School of Science
Department of Physics and Astronomy
Master Degree in Physics

Nucleation and growth of iron nanoparticles by gas phase condensation

Supervisor:
Prof. Luca Pasquini

Co-supervisors: Prof. Enrico Ghedini, Dr Giorgio La Civita

Submitted by:
Nicolò Canestrari

Academic Year 2020/2021

ACKNOWLEDGEMENTS

I am very thankful first and foremost to professor Luca Pasquini, professor Emanuele Ghedini and Dr Giorgio La Civita, all of them from University of Bologna, as well as to Dr Nicola Patelli and Dr Francesco Orlandi, for the support that has made possible the present work.

Special thanks also go to my family for the strong encouragement and to all the great teachers who helped my journey.

CONTENTS

Chapter 1

INTRODUCTION

Iron nanoparticles have a great range of applications, particularly in the medical and laboratory fields and even in treating environmental contaminations due to chlorinated organic compounds. Due to their particularly strong magnetic properties, including superparamagnetism which makes them good for spintronics applications, they are used in hard-disks and resonance imaging. Their high surface area give them a reactivity that permits a very important chemical application: as catalysts of processes that involve breaking or making a carbon-carbon bond. They are used in certain alloys, in plastics, in coatings, and can help the formation of carbon nanotubes.

Due to the great promises of this and other kinds of metal nanoparticles as well, there is a great deal of research on their methods of industrial production, and particularly strong is the interest in plasma reactors that optimize their nucleation, growth and collection: examples include the study of inductively coupled thermal plasmas in the production of platinum nanoparticles or of radio-frequency induction thermal plasma in the synthesis of silicon nanoparticles, as well as a huge variety of other researches.

Less strong is the use of computer simulations to understand the functioning of Gas Condensation Chambers, which is what the present work tries to do, adopting as a physical model classical nucleation theory. Whether in the study of planetary formation or of plasma dynamics computer simulations are a vital tool, and this is also completely true when it comes to the use of classical nucleation theory. We will present a comparison with experimental observations discussing the limitations and criticalities of the computational approach.

Chapter 2

GAS PHASE CONDENSATION

2.1 Classical nucleation theory

Nucleation is the process by which clusters of a stable phase form in a metastable phase. The formation of a new phase by a discontinuous phase transformation (such as the formation of a solid from a liquid or the precipitation of a solute-rich solid phase from a supersaturated solid solution) requires the nucleation of the new phase in highly localized regions of the system (see "Kinetics of Materials", Robert W. Balluffi, Samuel M. Allen, Craig W. Carter).

When dealing with the transformation of a bulk material the whole process of nucleation is divided in four stages:

1) The first stage is the incubation period in which the matrix phase is metastable and no stable particles of the new phase have formed. Nevertheless, small particles (termed clusters or embryos) which are precursors to the final stable phase continuously form and decompose in the matrix. The distribution of these clusters evolves with increasing time to produce larger clusters which are more stable and therefore less likely to revert back to the matrix. Eventually, some of the largest of these clusters evolve into particles (i.e., stable nuclei) of the new phase, remain in the system permanently, and continue to grow. At this point nucleation is well under way.

2) The second stage is the quasi-steady-state nucleation regime. During this period, the distribution of clusters has built up into a quasi-steady state and stable nuclei are being produced at a constant rate.

3) The third stage shows a decreased rate of nucleation to the point where the number of stable particles in the system becomes almost constant. This is commonly due to a decrease in the supersaturation (or free energy) which is driving the nucleation in untransformed regions of the system.

4) The fourth stage is the late period where the nucleation of new particles becomes negligible. However, many of the previously nucleated larger particles grow at the ex-

pense of the smaller particles in the system. This causes the total number of particles to decrease.

Since we are interested in nucleation happening in a chamber where an atmosphere is maintained in our case these different steps of the process can be understood as located in different places along the flux of vapour coming from the powder material, the fluidodynamics of the system being what governs the presence of supersaturated vapour. The study of this kind of nucleation is connected to the study of aerosol, meaning a dispersion of liquid or solid droplets in a gas, with particles mostly between 1μm and 1nm, which has a variety of applications to problems ranging from industrial synthesis to environmental concerns (see "Dust, Smoke and Haze", Friedlander). It is in relation to the growth of already nucleated clusters that we will use the Method of Moments and related concepts that are central to the study of aerosol and vital to the modeling of plasma reactors for the industrial production of nanoparticles.

The kind of nucleation mechanism we will consider is the homogeneous one, meaning that there is no edge or surface that helps the formation of our nanoparticles as often is the case in other kinds of situation: the heating and consequent formation of supersaturated vapour is supposed to do all the work here.

The process of nucleation depends on the balance between the free energy change associated to the surface tension and that associated to the bulk. If we have a system that consists initially of a certain number of atoms of a given chemical species in a parent phase (iron vapour, in this case) that is metastable with respect to the formation of an equilibrium phase, then according to the classical model, in order to nucleate the new phase, it is necessary for some of the metastable phase to be converted into small clusters of the new one and, in turn, for at least some of these clusters to survive possible conversion back to vapour (dissolution). The small clusters will have a large surface-to-volume ratio, and their interfacial energies will therefore be relatively large. This relatively large interfacial energy will make the formation of small clusters difficult and act as a barrier to the nucleation.

If a cluster is produced, its total energy, in the classical model, is assumed to be separable into bulk free energy and interfacial free energy terms. If the energy of the cluster/matrix interface is isotropic and no elastic strain energy is present, the free energy change due to the formation of the cluster is then written

$$\Delta G_N = \Delta G_{bulk} + \Delta G_{surface} \tag{2.1.1}$$

which is developed as:

$$\Delta G_N = N(\mu_{new} - \mu_{old}) + \eta\gamma N^{2/3} \tag{2.1.2}$$

where ηis a shape factor and γis the energy per unit area, that is the surface tension factor which depends on the chemical species. The first term is due to the difference in chemical potential between the new and old phase (which is supposed to be negative)

and it goes with the number of atoms that compose the cluster while the second term increases less with such number, so that the great obstacle toward the nucleation of a new phase is given by the formation of the first stable clusters.

By imposing that the derivative of the free energy change given by eq. (2.1.2) be null we arrive at the following conditions for a stable nucleus to form, after a continuous process of formation and dissolution of smaller nuclei:

$$N_c = \frac{8}{27}(\frac{\eta\gamma}{\mu_{old} - \mu_{new}})^3 \tag{2.1.3}$$

$$\Delta G_c = \frac{1}{3}\eta\gamma(N_c)^{2/3} \tag{2.1.4}$$

These equilibrium conditions given by eq. (3) and (4) are then relevant in modeling the quasi-steady state:

Under thermodynamic equilibrium conditions one can write:

$$\frac{{n_N}^{eq}}{n} = e^{-\frac{\Delta G_N^{eq}}{kT}} \tag{2.1.5}$$

for the number of clusters having a certain number N of atoms. Then three main assumptions are made: that between clusters with less atoms than the critical number of eq. (2.1.3) a detailed balance is achieved, that clusters are allowed to grow way beyond this critical number and that eq. (2.1.5) can be rewritten as:

$$\frac{{n_N}^{eq}}{n} = e^{-\frac{\Delta G_N}{kT}} \tag{2.1.6}$$

substituting the free energy change under equilibrium condition with that determined by the other two assumptions: this is also known as the "constrained equilibrium hypothesis".

One can also write, for the 'fluxes' between clusters of different size:

$$J_N = A_N n_N - L_{N+1} n_{N+1} \tag{2.1.7}$$

which at any given time gives the number of clusters going from having N atoms to N+1, the first term being the one that accounts for absorption of one atom while the second accounts for the loss of it.

Finally using eq. (2.1.6), making a first order expansion of the coefficients of eq. (2.1.7), and integrating under quasi-steady conditions while replacing the free energy change with an expansion around that of eq. (2.1.4), one gets:

$$J = Z A_c N_s e^{-\frac{\Delta G_c}{kT}} \tag{2.1.8}$$

with

$$Z = \sqrt{\frac{\Delta G_c}{3\pi {N_c}^2 kT}} \tag{2.1.9}$$

where Z is the Zeldovich factor, typically around 1e-1, and the rate of nucleation J is also dependent on the number of nucleation sites and the probability of an atom to join the nucleus.

The physical situation to which we apply this model is on one hand very simple lacking complications like that of chemical reaction, or of the effect of strain energy we could find in a solid; on the other hand the very high supersaturation we expect to see in order for nucleation to rapidly occur could make for some difficulties.

2.2 Gas condensation chamber

The Gas Condensation Chamber (GCC) is the most used laboratory technique to synthesize nanocrystals: it works by heating a powder material up to vaporize it in an inert atmosphere (we will consider He and Ar) where they will move by convection toward a cold cylinder (kept at low temperature by the use of liquid nitrogen) and will deposit there as dust. When time comes for this dust to be collected and analyzed an ultra-high vacuum is created (1e-7 Pa) to avoid contamination while the cylinder is scraped and the dust is collected below, compressed and extracted. One of the key differences between this situation and that of the plasma reactors that are often considered in industrial research is that there avoiding the deposition of nanoparticles on the walls is an optimization parameter, while here we aim at collecting the deposited dust.

The GCC can also be used in studying alloys, by using more than one powder material, positioning them on separate crucibles where they are heated and the vapours mix. Another alternative is to use it with a reactant atmosphere as one does to produce metal-oxide nanoparticles that are of great importance in the study of ceramic materials and in various other applications (see "One-Step Synthesis of Metal/Oxide Nanocomposites by Gas Phase Condensation", Nicola Patelli, Andrea Migliori, Vittorio Morandi, Luca Pasquini). In general, nanoparticles of different dimensions can be obtained varying the incoming flux, the pressure and most of all the temperature, which is why a better understanding of the way this technique works could help improve its functioning. In order to get an even more precise control on the nucleation process some possibilities are the use of laser-ablation techniques, of electron guns and of ion guns.

In our case the chamber (see fig. 2.1 and 2.2) works at 260 Pa, with an incoming flux of 5 mln/h and with the single powder material, iron, heated on the crucible at a temperature that will be assumed to be 2100K, over the 1808K required to melt iron, because at this temperature the production rate of iron nanoparticles is relevant for practical application, while close to the melting point the nanoparticles yield is generally

very low. Based on the data collected during the functioning of the chamber, the iron nanoparticles produced have a dimension of 2 nm to 15 nm when an Helium atmosphere is employed, up to 50 nm when an Argon atmosphere is employed.

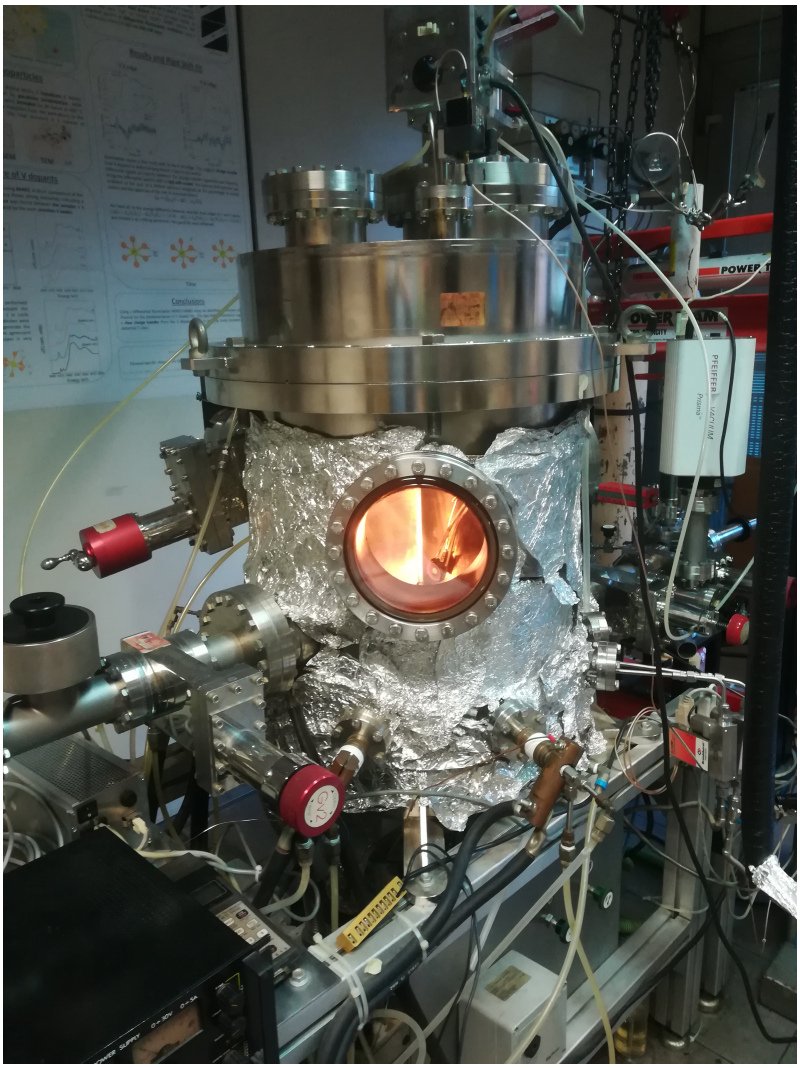

Figure 2.1: Chamber

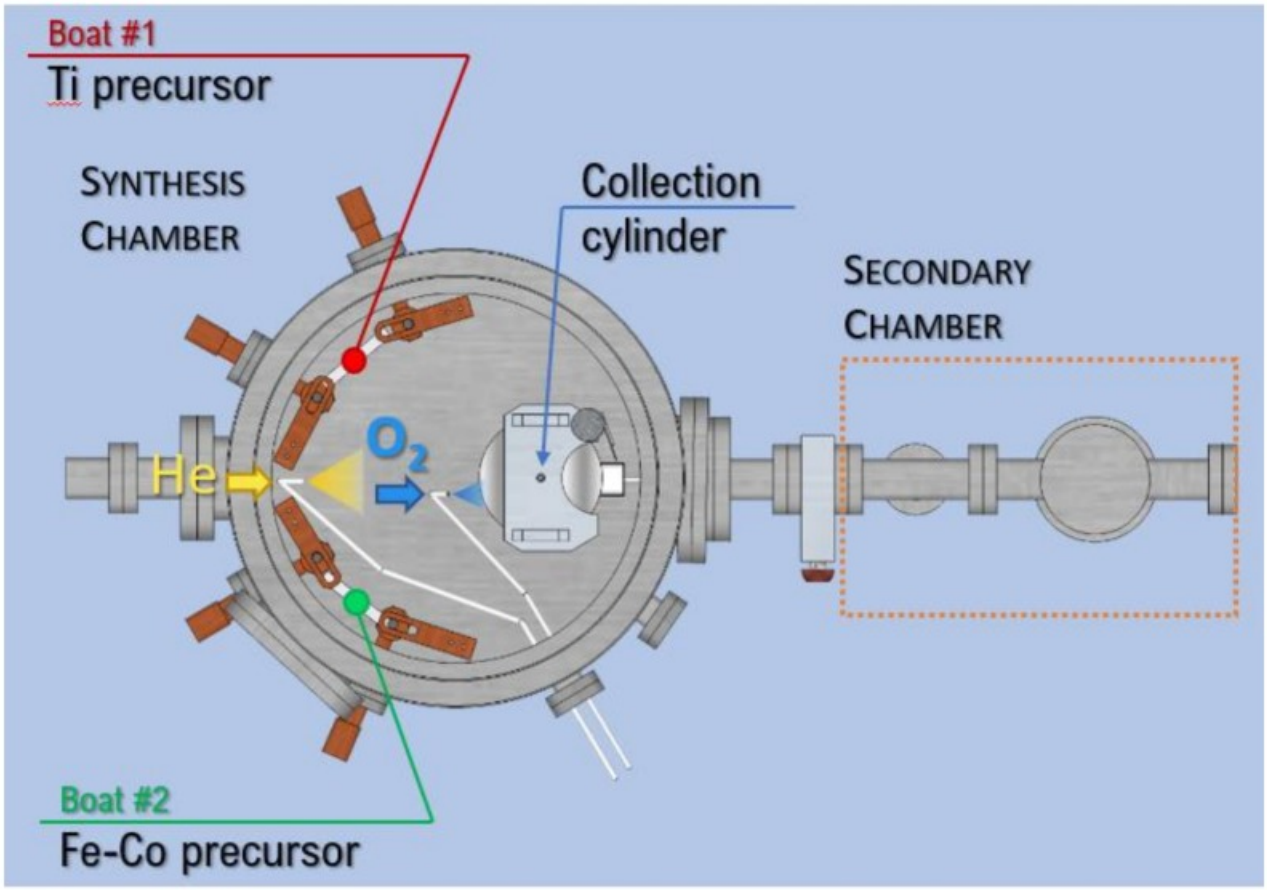

Figure 2.2: Chamber: here represented while producing metal/oxide nanocomposites

Chapter 3

SIMULATIONS

3.1 The software

ANSYS FLUENT (version 19.2, see ANSYS manual) is one leading commercially available software for computational fluid dynamic (CFD) simulations: the domain is discretised into a finite set of control volumes and partial differential equations that govern transport of mass, energy and chemical species in the fluid are converted into algebraic equations and then solved numerically.

We will accept as a limitation that the physical problem must be confronted as bidimensional. The solver (pressure-based) will be used in a steady mode with the equations of continuity, energy, momentum, composition and those required by the turbulence model adopted to be solved simultaneously on a mesh that will be more refined near the crucible where we expect nucleation to happen. Due to the lack of a unique right way to describe fluid dynamic the solutions adopted can only be at least in part the result of a trial and error process of selection.

The adopted system of equations is similar to that of Navier-Stokes but we will consider a compressible fluid with a chemical composition (but no chemical reactions); it can nevertheless be observed that the knudsen number of the system is

$$Kn = \frac{k_b T}{\sqrt{2}\pi\sigma^2 PL} < 0.01 \tag{3.1.1}$$

where sigma is the atomic diameter and L the relevant dimension, which implies, despite the very low pressure (P) of the chamber, a viscous fluid regime.

The following equations are loaded on the solver:

$$\frac{\delta\rho}{\delta t} + \nabla\rho u = 0 \tag{3.1.2}$$

$$\frac{\delta\rho u}{\delta t} + \nabla\rho uu = -\nabla p + \nabla\tau \tag{3.1.3}$$

$$\frac{\delta[\rho(e+\frac{1}{2}u^2)]}{\delta t} + \nabla[\rho u(e+\frac{1}{2}u^2)] = \nabla(k\nabla T) + \nabla(-pu+\tau u) \tag{3.1.4}$$

where u is velocity vector, k thermal conductivity and tau the viscous stress tensor. To these others will be added in specifying the model.

At the core of the computational method of dealing with Navier-Stokes like, discretised systems of equations is the iteration of provisional solutions, step by step, until a result is reached that doesn't greatly differ from the precedent, the limit of such an acceptable difference being given by the convergence criteria established for the simulations and the whole process being monitorable by looking at the trend of the residuals. For our simulations we use a 0.0001 convergence criteria for all residuals (not reached).

In order to avoid a rapid onset of an unstable solution patterns, ANSYS FLUENT provide for under-relaxation factors which will be set at 0.3 for pressure, 0.4 for composition, 0.7 for energy, accepting for other residual the default, based on an empirical handling of the system: this way only a proportionally limited part of a result will be taken as valid for the next iteration.

3.2 The virtual chamber

The chamber will be taken as bidimensional consisting in the plane where both the cylinder and the crucible lay; we draw it based on the following taken measures: inside the chamber which is 50 cm wide and 60 cm high we draw the cylinder 15 cm wide and 30 cm high, the crucible 0.5 cm wide and 1.5 cm high, inlet and outlet just 0.5 cm wide. The mesh (see fig. 3.1 and 3.2)) we introduce through a series of refinements so that it is particularly thin near the crucible.

The flux (right to left in figures) will be given by an inlet velocity of 20 m/s, corresponding to 5 mln/h, a relatively low process of atmospherical recycle. At the outlet we only specify the requisite that pressure being the one established for the chamber, which is 260 Pa. Gravity is imposed inserting the usual earth constant g.

We put the cylinder at a temperature of 70 K, inside the range of liquid nitrogen, and the crucible at 2100 K, above the iron melting point, though we lack a precise measurement of temperature due to the difficulty of inserting a thermocouple in the chamber. Temperature enters the energy equation (3.1.4) and so does energy due to the gravitational field. As for heat transfer only thermal conduction will be considered, according to the properties of the materials, while radiative heating will be ignored.

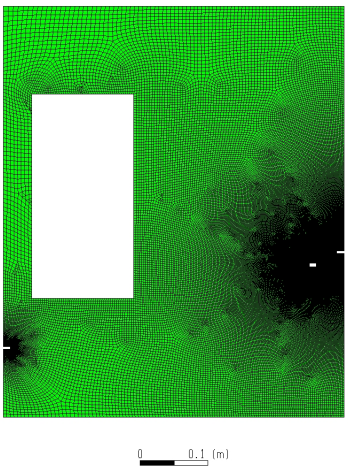

Figure 3.1: The mesh: full view

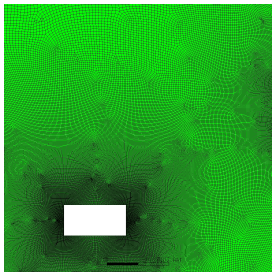

Figure 3.2: The mesh: detail near the crucible

3.3 Modeling materials

We are interested in describing the atmosphere, so the cylinder, the crucible and the walls will enter our simulation only due to the surface specifications of temperature and, for the crucible, composition.

In the material panel of ANSYS FLUENT a mixture is set up of Argon (or Helium) as prevalent element and (atomic) Iron, and as for the properties of such mixture a rule of mass weight combination is given, while properties of each component are specified independently. Helium and Argon are assigned their atomic masses and a specific heat of respectively 5193 and 520.64 in MKS units, while thermal conductivity is set up to be computed according to kinetic theory; Iron is assigned a specific heat of 900 and kinetic theory is set up for other properties.

It is to be specified that the density of the mixture follows the ideal gas law, which will be accounted for in solving the continuity, flow and energy equations.

The Lennard-Jones parameters also are required for the set up of the mixture and specifically for the computing of viscosity and thermal conductivity according to kinetic theory: we have L-J characteristic length and energy parameter of 3.451 (Armstrong) and 116 (K) for Argon, 2.628 and 5.465 for helium as one can find in literature (see e.g. "Modified Lennard-Jones Potentials with a Reduced Temperature-Correction Parameter for Calculating Thermodynamic and Transport Properties: Noble Gases and Their Mixtures (He, Ne, Ar, Kr, and Xe)", Journal of Thermodynamics, Volume 2013, Article ID 828620, Seung-Kyo Oh). The Lennard-Jones potential is the most frequently applied model in molecular simulation history because it was, and most likely still is, the best trade-off between computational cost, accuracy, and compatibility even when compared to the LJTS model (see "How well does the Lennard-Jones potential represent the thermodynamic properties of noble gases?" MOLECULAR PHYSICS 2016, VOL.0, NO.0). (see also, as for the L-J parameters to model iron, "Parameters (sigma, epsilon) of Lennard-Jones for Fe, Ni, Pb for Potential and Cr based on Melting Point Values Using the Molecular Dynamics Method of the Lammps Program", C Y Maghfiroh et al 2020 J. Phys.: Conf. Ser. 1491 012022).

The species transport model is set up including thermal diffusion, which will cause lighter particles to diffuse more rapidly toward heated surfaces and the reverse for heavier particles (iron atoms, here) according to the Ludwig-Soret effect (thermophoresis), while there is no need of the inlet diffusion option, which would imply an immission of metal vapour at the entry: we expect the massive/molar fraction of iron in the chamber to be computed from the boundary condition at the hot-inlet (up surface of the crucible).

The massive fraction of iron near hot-inlet is determined according to vapour pressure equilibrium:

$$\frac{P_{fe}}{P_{he/ar}} = \frac{n_{fe}}{n_{he/ar}} \tag{3.3.1}$$

where we can assume helium/argon pressure to be equal to that of the chamber (260 Pa) while iron vapour pressure can be determined according to:

$$\log \frac{P_{fe}}{P_{atm}} = 6.347 - \frac{19574}{T} \tag{3.3.2}$$

considering we have T higher than 1808K, melting temperature of iron, and using the semi-empirical Antoine equation which here holds even considering extensions by additional parameters: those are null in this case (see "Metal vapour pressure" table mmrc.caltech.edu). Applying eq. (3.3.1) and (3.3.2), and factoring the different atomic weight, leads to values of 48% and 96% for atmospheres of argon and helium respectively.

3.4 Turbulence

If we consider a simple incompressible pipe flow, its properties can be described as laminar or turbulent depending solely on the Reynold number which one can see as dividing the viscous part in the last term in eq. (12): we have

$$\frac{\delta u}{\delta t} = -\nabla p + \frac{1}{Rey}\nabla^2 u \tag{3.4.1}$$

without considering external forces, where we put

$$Rey = \frac{\rho L u_{mean}}{\eta} \tag{3.4.2}$$

where eta is the viscosity of the fluid. Were we considering a wind tunnel, such as those used in aerodynamic tests, we simply would have to pick the right length scale L and then decide between turbulent and laminar flow depending on whether Rey is higher or lower than approximately 2300, with numbers between 2300 and 2900 being an intermediate case: in this case Rey would be far lower.

For compressible fluids the mach number, given by the ratio of velocity over speed of sound, also permit to distinguish different flow regimes, and that would still allow for our case to be treated as laminar, considering in particular the low inlet velocity: 20 m/s with speed of sound being approximately 319 m/s for Argon and 1007 m/s for Helium at room temperature.

What we have here is a compressible gas which, while circulating in the chamber, is kept between the temperatures of the crucible (2100K), of the cylinder (70K) and of the walls (300K), also subject to gravity. Therefore one could also study the possibility of a convection cell or other peculiarity of circulation depending on the linked effects of density variation and heat transfer. Turning to the Rayleigh-Bérnard convection mechanism as a model for what we may see in the chamber we can introduce the Rayleigh number:

$$Ray = \frac{g\beta}{\nu\alpha} L^3 (T_{hot} - T_{cold}) \tag{3.4.3}$$

where g is earth gravity, L is the eight of the container (the chamber here), the temperature differential is taken between the crucible and the upper wall, though one may also consider the role of the cylinder, and

$$\beta = \frac{1}{V}(\frac{\delta V}{\delta T})_p \tag{3.4.4}$$

$$\nu = \frac{\eta}{\rho} \tag{3.4.5}$$

$$\alpha = \frac{k}{\rho c_p} \tag{3.4.6}$$

are respectively the thermal expansion coefficient, the kinematic viscosity, and the thermal diffusivity. The transition from laminar to turbulent flow is here supposed to take place for

$$10^8 < Ray < 10^{10} \tag{3.4.7}$$

(see ANSYS FLUENT 12.0 Theory Guide-5.2.2 Natural convection and Buoyancy-driven Flows Theory)

Using known data for density, thermal conductivity and viscosity at room temperature, controlling for pressure, we have Ray for helium around 10000, as an order of magnitude, while for Argon it's nearer to 100000 mainly due to higher density; for comparison the critical condition for convection for rigid-rigid boundaries is 17610.39, though of course our problem also include the circulation dependent on the given inlet velocity.

Given a Rayleigh number much lower than the lower limit of condition (3.4.7) we don't really expect to see a great deal of turbulence; still we decide to include in the simulation a model of turbulence that is thought to work well where the convective cell could develop and so could some instabilities. So we know that the two preferred models adopted for turbulent stream are the k-w and k-epsilon, both available to the ANSYS FLUENT user: the k-w model will be adopted in that it works better away from edges which is where we may see some turbulent dynamics due to convection.

The k-w turbulence model consists in the following two equations:

$$\frac{\delta(\rho k)}{\delta t} + \frac{\delta(\rho k u_i)}{\delta x_i} = \frac{\delta(\Gamma_k \frac{k}{x_j})}{\delta x_j} + G_k - Y_k + S_k \tag{3.4.8}$$

$$\frac{\delta(\rho w)}{\delta t} + \frac{\delta(\rho w u_i)}{\delta x_i} = \frac{\delta(\Gamma_w \frac{w}{x_j})}{\delta x_j} + G_w - Y_w + S_w \tag{3.4.9}$$

In these equations, G_k represents the generation of turbulence kinetic energy due to mean velocity gradients. G_ω represents the generation of ω. Γ_k and Γ_ω represent the effective diffusivity of k and ω, respectively. Y_k and Y_ω represent the dissipation of k and ω due to turbulence. S_k and S_ω are user-defined source terms which we will set to zero. The physical meaning of the two terms k and w is respectively that of turbulent kinetic energy and rate of dissipation: conversion of that into thermal energy.

The low-Reynolds number correction can be seen in the following term:

$$\mu_t = \alpha_* \frac{\rho k}{w} \tag{3.4.10}$$

where:

$$\alpha_* = \alpha_(inf)(\frac{\alpha_0 + \frac{Re_t}{R_k}}{1 + \frac{Re_t}{R-k}}) \tag{3.4.11}$$

$$Re_t = \frac{\rho k}{\mu w} \tag{3.4.12}$$

$$R_k = 6 \tag{3.4.13}$$

$$\alpha_0 = 0.024 \tag{3.4.14}$$

which then enters in the equations for Γ_k and Γ_ω:

$$\Gamma_k = \mu + \frac{\mu_t}{\sigma_k} \tag{3.4.15}$$

$$\Gamma_w = \mu + \frac{\mu_t}{\sigma_w} \tag{3.4.16}$$

This way it is obtained that turbulent viscosity (3.4.10) gets dumped where the turbulent Reynolds number is low. Here σ_k and σ_ω are the turbulent Prandtl numbers for k and ω, giving the ratio between momentum and thermal eddy diffusivity.

The setting up of this turbulence model requires to specify additional boundary conditions at the inlet: turbulence intensity and turbulence viscosity ratio, both referred to the incoming fluid. We leave turbulence intensity, given by the ratio of the root-mean square of velocity fluctuation to the mean velocity, at 5% following the default setting: we expect to find then an higher value for it given the strong negative dependency of it on Reynolds number. As for turbulence viscosity ratio we accept the given value of 5, which is inside the most typical range from 1 to 10.

3.5 Nucleation

We aim to explain the formation of nanoparticles which makes it necessary to introduce a program for the conversion of vapour into clusters of atoms in the first place and then the condensation and growth of those clusters and the coagulation of them. We first introduce, after running some simulations without nanoparticles formation, a C++ program for the nucleation of the initial clusters from vapour. Here we report some salient lines of code:

```
real sigma_ts(real T){ /* surface tension - HARDCODED for Fe */

  real sigma;
sigma = 1.92-3.97*(T - 1811.0);

  if (sigma < 0.1)
    sigma = 0.1;

return sigma;
}
```

where we include the surface tension of iron given according a two parameters equation, 1808K being the melting temperature of iron, for which we use as source "Surface tension of nickel, copper, iron and their binary alloys" (JOURNAL OF MATERIALS SCIENCE 40 (2005) 2213– 2216, J. BRILLO, I. EGRY).

```
real p_saturation(real T){ /* saturation pressure - HARDCODED for Fe */

  real Psat;

  if (T < 300.0)
T = 300.0;

  Psat = pow(10.,(6.347 -(19574.0/T)))*101000;

  return Psat;
}
```

Here we again insert the vapour pressure of iron already used to determine the composition.

```
real n_saturation(real T) { /*N_s, equilibrium saturation monomer concentration
at temperature T [molecules/m3] - Girshick Chiu McMurry 1990 */

real N_s;

    if (T < 300.0) T = 300.0;

N_s = p_saturation(T) / (K_BOL*T);

return N_s;
}
```

Here is the correspondent concentration of atomic nuclei, easily computed for a given temperature and an important factor in determining the size of particles produced as one can see in the cited article, where a plasma reactor is considered.

The program is used in compiling a user-defined function with ANSYS, loading a library that is then used for the simulation. When the proper physical conditions are reached, according to classical nucleation theory, particularly due to the surface tension of iron influencing the free energy with which the nucleation rate varies exponentially, it is computed that clusters will form at a certain rate, and on the condition (necessary for stability) that they do possess a minimal critical volume.

```
/* Nucleation rate I [#/m3 s] and critical volume v_crit [m3] */
     real n_v = C_YI(c,t,spe_vap)*C_R(c,t)*N_AVO*1000./M_si;
     if(n_v<1.0) n_v = 1.0;

     real p_vap = n_v*K_BOL*T;

     real S = 1.;
     if(n_s>1) S = n_v/n_s;

     real ST_norm = sigma_ts(T)*s_mon/(K_BOL*T);

            real I = 0.0;
            real v_crit = v_mon; /* lower limit for v:crit is the monomer volume */

         if(S>1.) {
         v_crit = (M_PI/6.0) * pow((4.0*sigma_ts(T)*v_mon)/(K_BOL*T*log(S)),3.0);
         I = (4*s_mon*sqrt((K_BOL*T)/(M_PI*M_mon))*n_s*n_v) / 12.0*
             sqrt(ST_norm / (2.0*M_PI))
             *exp(ST_norm - (4 * pow(ST_norm, 3.0)) / (27.0*pow(log(S), 2)));
         }

 /* vapour phase source term */
         C_UDMI(c,t,udm_mom_vap_nucl) = - I * (v_crit/v_mon) * M_mon;
 /* monomer sink by nucleation [kg/m3 s] */
```

The program also gives the initial diameter of newly nucleated particles:

```
printf("Diametro medio primarie %e\n",2*pow(3*(num/den)/(4*M_PI),1./3.));
```

where *num* and *den* are adjusted while the program cycles like other user-defined memories storing various important informations:

```
 C_UDMI(c,t,udm_mom_v_crit) = v_crit;

 C_UDMI(c,t,udm_mom_I) = I;

 /* vapour phase source term */
 C_UDMI(c,t,udm_mom_vap_nucl) = - I * (v_crit/v_mon) * M_mon;
 /* monomer sink by nucleation [kg/m3 s] */

/* Storing variables */
    C_UDMI(c,t,udm_mom_n_v) = n_v;
```

```
C_UDMI(c,t,udm_mom_p_vap) = p_vap;
C_UDMI(c,t,udm_mom_p_sat) = p_s;
C_UDMI(c,t,udm_mom_S) = S;
C_UDMI(c,t,udm_mom_n_s) = n_s;

num += C_UDMI(c,t,udm_mom_I)*C_UDMI(c,t,udm_mom_v_crit);
den += C_UDMI(c,t,udm_mom_I);
```

Here the user-defined memories records the critical volume for the formation of a particle, the nucleation rate, the vapour sink, the monomer concentration, the vapour pressure, the saturation pressure, the saturation ratio and monomer equilibrium concentration at saturation. User-defined memories are then enumerated according to the header file and accessible in display.

3.6 Simulating an Argon atmosphere

A simulation is run with an Argon atmosphere modeled as described; 6000 iterations are made (see fig.3.3). We can see a certain pattern being reached even if the criteria of convergence are not met. The profiles of velocity magnitude and temperature (see fig. 3.4 and 3.5) give an idea of the circulation inside the chamber where one can note the effect of heating in generating an upward flux and the way this influence temperature profile, particularly in the zone over the crucible.

A confirmation of the reasonableness of these results has been made, verifying that pressure is uniform in the chamber, and that density varies with temperature, as well as the fact that viscosity and thermal conductivity (fig. 3.9 and 3.10) correctly depend on temperature. Also the same results for velocity and temperature have been obtained by a different simulations, changing the turbulence model by eliminating the low-Rey correction.

As a result of the adopted turbulence model we have profiles (fig. 6-8) of turbulent energy, turbulent intensity, turbulent viscosity and turbulent Reynolds number, all of them showing the development of some form of convective process due to the heating.

The profile for iron mass fraction (fig. 3.11) also has been observed to be reliable, and the confinement of iron vapour near the crucible cannot be said to depend on nucleation, as one can see in fig. 3.18, since the program adopted is not such that eliminates iron atoms from the chamber. The program gives a mean diameter for formed nanoparticles of 3.5e-10 which is only slightly more than the iron atom diameter, but of course other processes such as condensation and coagulation will have to be accounted for in order to compute nanoparticles size. Nonetheless the various nucleation related quantities, stored as user-defined memories, give a good qualitative idea of where the nucleation initially occurs.

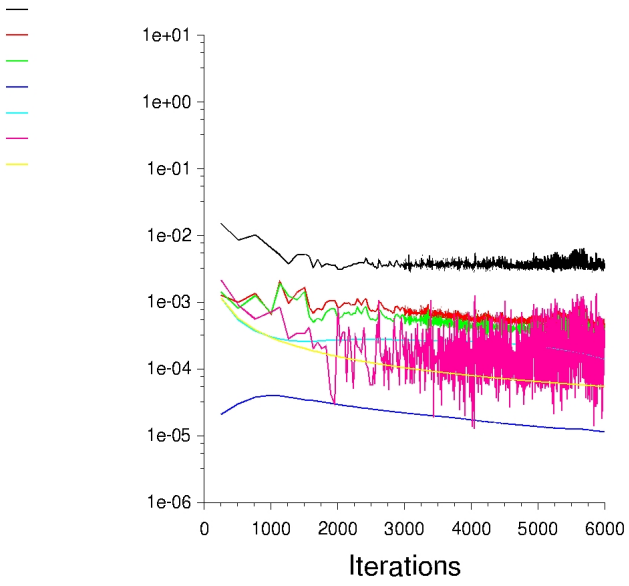

Figure 3.3: Residuals

The black, red and green represent the continuity equation (eq. 3.1.2), x-velocity and y-velocity (eq. 3.1.3), the light-blue and pink are k and w (eq. 3.4.8 and 3.4.9), the yellow and blue are composition (which includes thermal diffusion) and energy (eq. 3.1.4). The convergence criteria (1e-4) are not met except for the energy equation, but one can see anyway the emergence of a stable pattern, where the w (dissipation rate) residual is the one that most oscillates due probably mostly to difficulties in sorting out calculation at the edges.

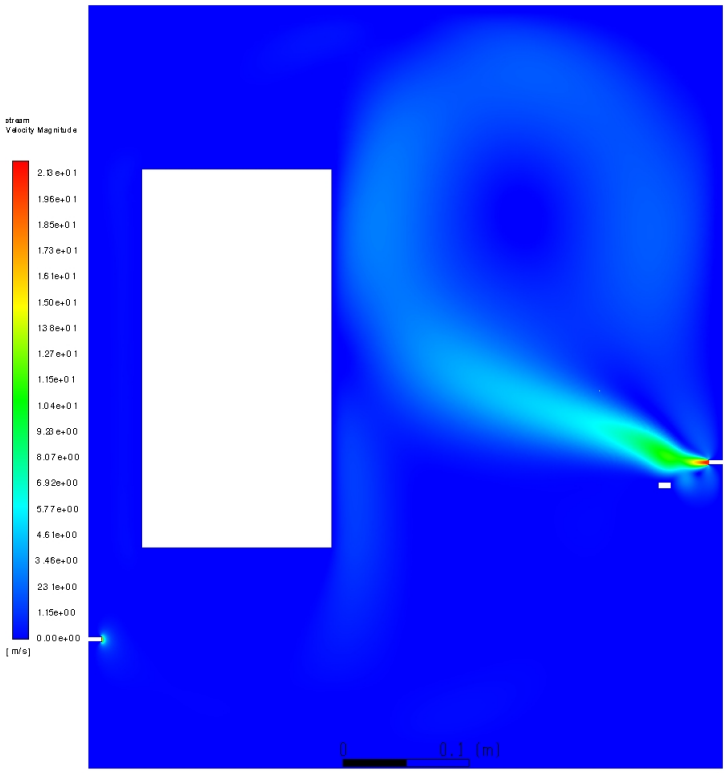

Figure 3.4: Velocity magnitude

It is shown here that immediately after entering the chamber the Argon jet is heated and a stream is generated that first goes upward and then widens, also partly falling down on the left, though one can also see the circulation over the inlet due to the falling of previously heated gas. Velocity varies between zero and a little more of the given entry velocity; the 'flame' immediately out of the pipeline also shows a proper curved profile due to viscosity: sometimes CFD simulations are made giving also a profile of inlet velocity, which we did not.

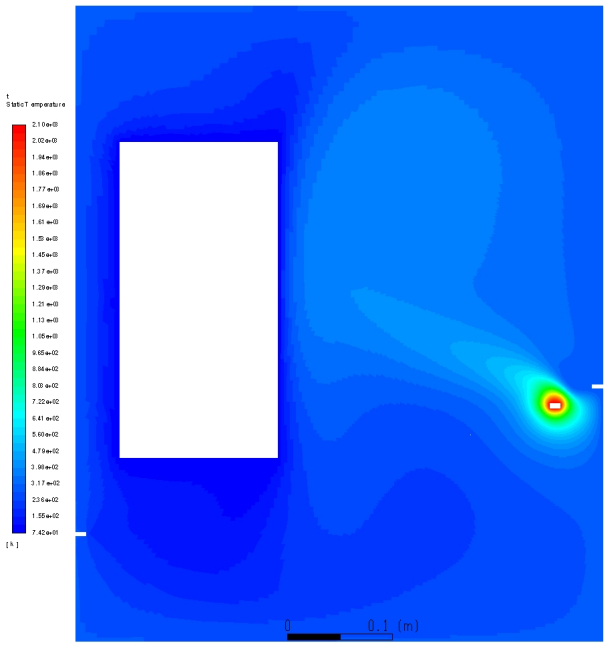

Figure 3.5: Temperature

Temperature follows a profile similar in some regards to that of velocity: the tip from the crucible pointed up and left can be understood as a dragging due to the incoming flux. The temperature gradient is very high near the crucible, with a fast cooling, and higher on the right of it. The temperature at the walls was fixed at 300 K, despite the empirical proof of some heating: here it seems that near inlet some more heating could occur even without considering irradiation.

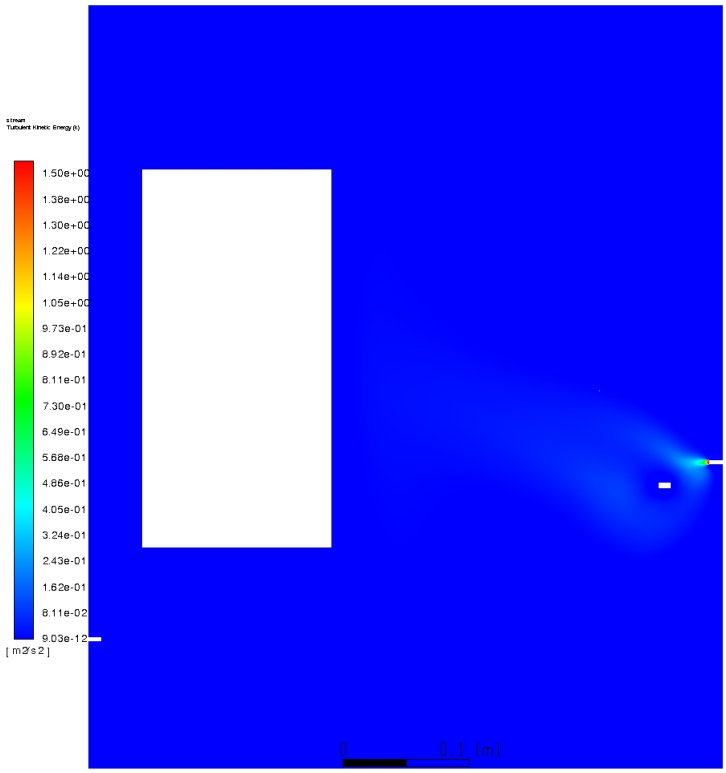

Figure 3.6: Turbulent kinetic energy

Turbulent kinetic energy gives the kinetic energy per unit mass associated with eddies, which means depending on the root-mean-square of velocity fluctuations. We see it varying from almost zero to 1.50 m^2/s^2 between inlet and the crucible, which still means that the kinetic energy of the entering flux outweighs it considerably.

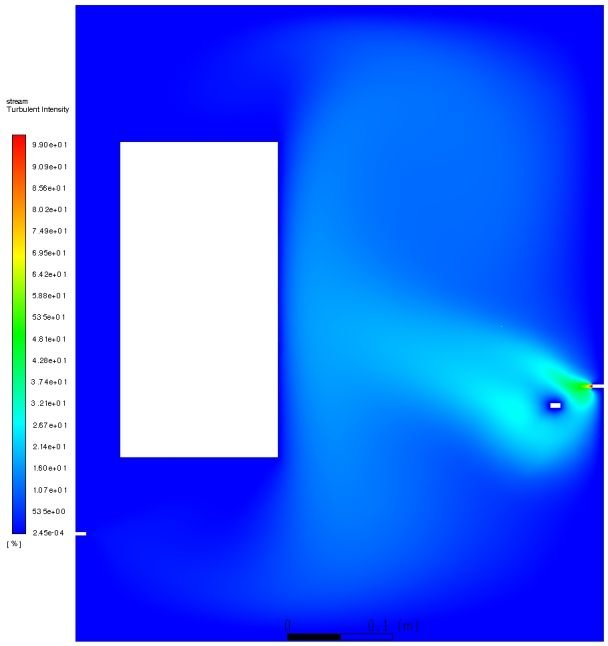

Figure 3.7: Turbulence intensity

Turbulence intensity is given by the root-mean-square of velocity fluctuations divided by mean velocity, so we can compare it to fig. 3.6 and fig. 3.4. It varies between almost zero and 99%: we observe peaks all around the crucible as well as a 'cloud' of turbulence while the value goes to zero near the crucible, as expected given the model adopted; compared with fig. 3.6, because of the dividing for velocity, we have a wider picture of turbulence in the chamber. There is no residual of the low value of turbulence given at the entry.

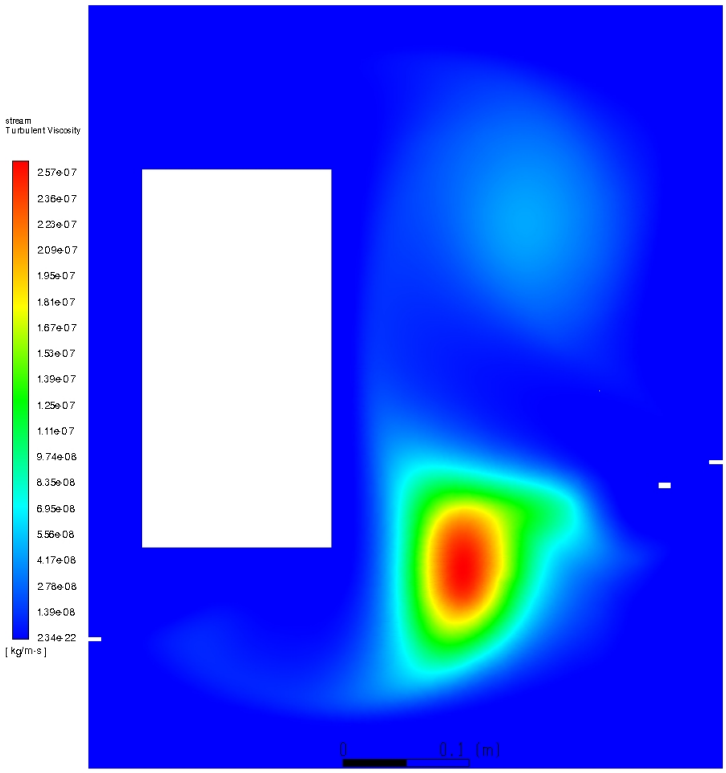

Figure 3.8: Turbulent viscosity

Turbulent viscosity, as we have it in eq. (3.4.10), is to be added to molecular viscosity (fig. 3.9) to give the total apparent viscosity. It varies here between almost zero to 2.5e-7 (MKS units), to be compared with molecular viscosity which can reach a value of 1.8e-4 but does not fall under 6e-6 and varies differently, meaning we have most of apparent viscosity in the center of the chamber due to turbulence. Considering eq. (3.4.10) and fig. 3.6 we can see how this value depends on the presence of turbulence in the middle between the crucible and the cylinder together with the fact that most dissipation take place on the edges. We also can see a 'cloud' of turbulent viscosity in the high part of the chamber between the cylinder and the wall, in agreement with what already seen with the velocity profile.

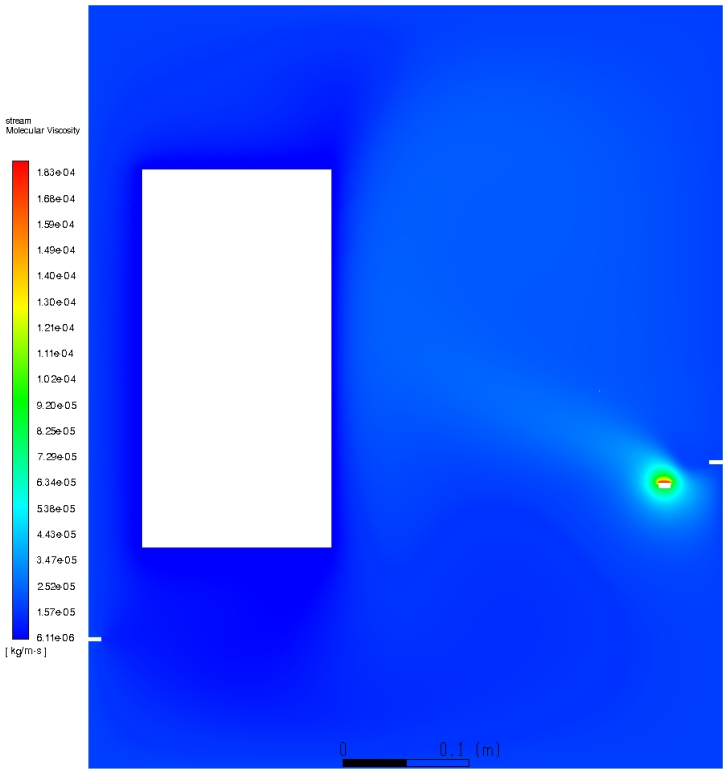

Figure 3.9: Molecular viscosity

Molecular viscosity varies in the range between 6.11e-6 and 1.8e-4 (MKS units), in a way which clearly depends on temperature as expected; since the higher value is reached near the crucible, where iron vapour is much relevant, this doesn't reflect Argon viscosity, which can be verified to be what we would expect from literature looking at the lower value.

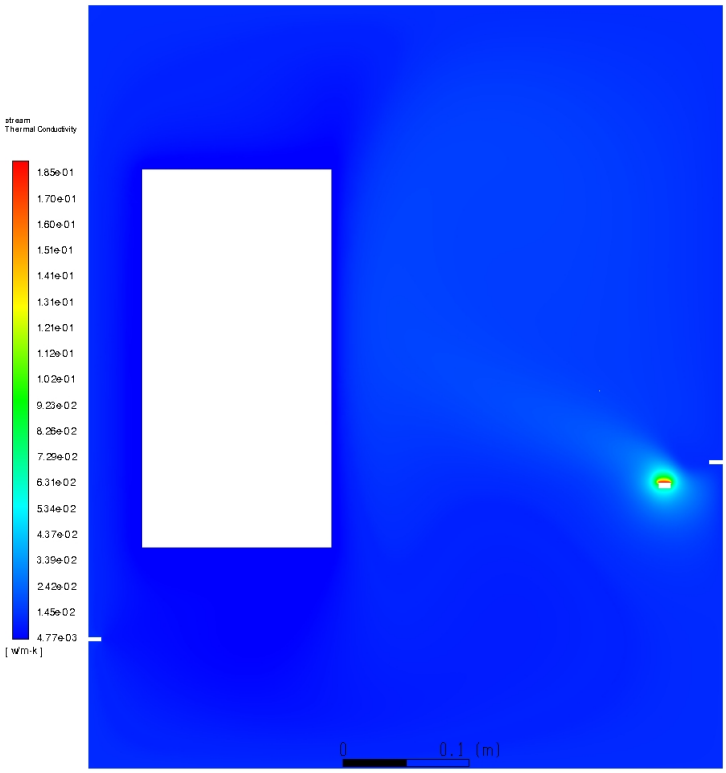

Figure 3.10: Thermal conductivity

We see for thermal conductivity the same profile observed for molecular viscosity, varying this time between 4.77e-3 and 1.85e-1 (MKS units). This is also compatible with the values reported in literature.

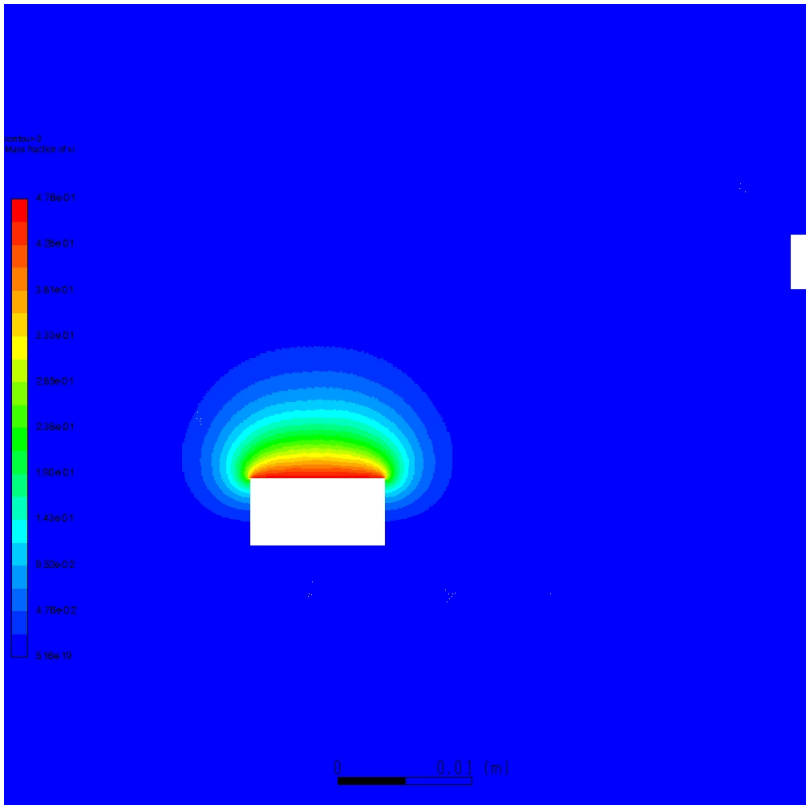

Figure 3.11: Composition: mass fraction of iron

The composition of the atmosphere near the crucible rapidly changes from that assigned immediately at the wall to an essentially pure Argon gas. As can be observed in fig. 3.18 this is not because of the formation of nanoparticles, since we don't actually make disappear the iron vapour. Attempts have been made to introduce a profile of composition near the wall because of the powder metal being confined in the center, which we didn't in the end, but we can say that the result here is a satisfactory one.

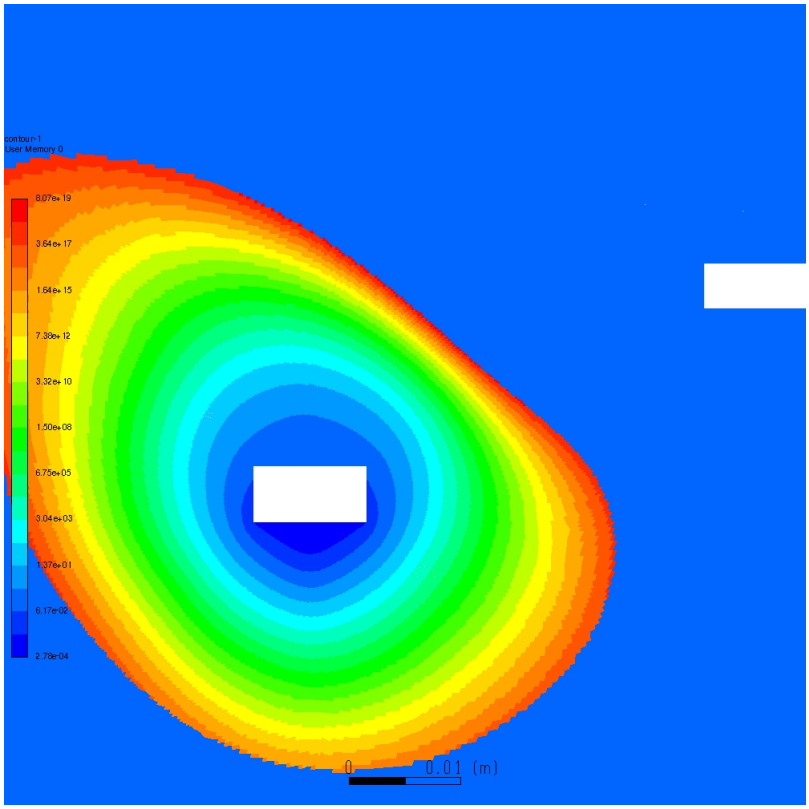

Figure 3.12: Saturation ratio

The saturation ratio is the ratio between the real concentration of iron atoms (monomers) and the concentration we would expect to see at equilibrium: according to classical nucleation theory it governs both the rate of nucleation and the minimum critical volume of stable nucleated particles. We observe supersaturation in the zone near the crucible up to 8.07e19 (the scale is logarithmic here).

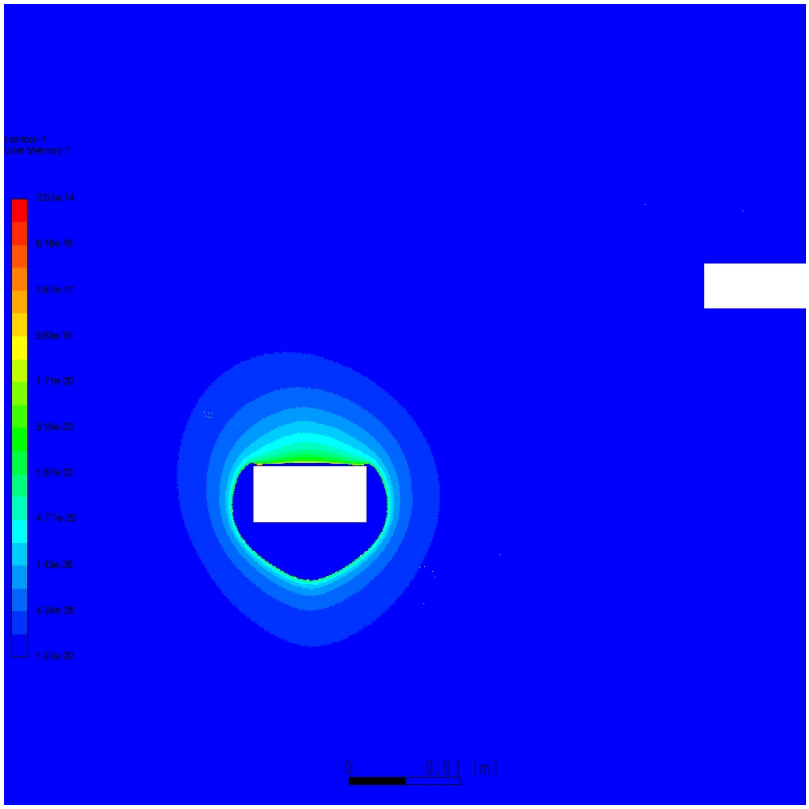

Figure 3.13: Critical volume (m^3)

Here we have, on a logarithmic scale from the monomer volume to 2.03e-14 the minimum particle volume for a stable nucleation: it shows a profile that matches that of the saturation ratio when this has just ceased to be negative and then steadily declines; the critical volume has been given a dependence on $log(S)^{-3}$ according to our model of nucleation, which means that it will be very high where the nucleation process begins to happen. Considering the low mean diameter computed, we expect that most particles nucleate indeed when critical volume has declined.

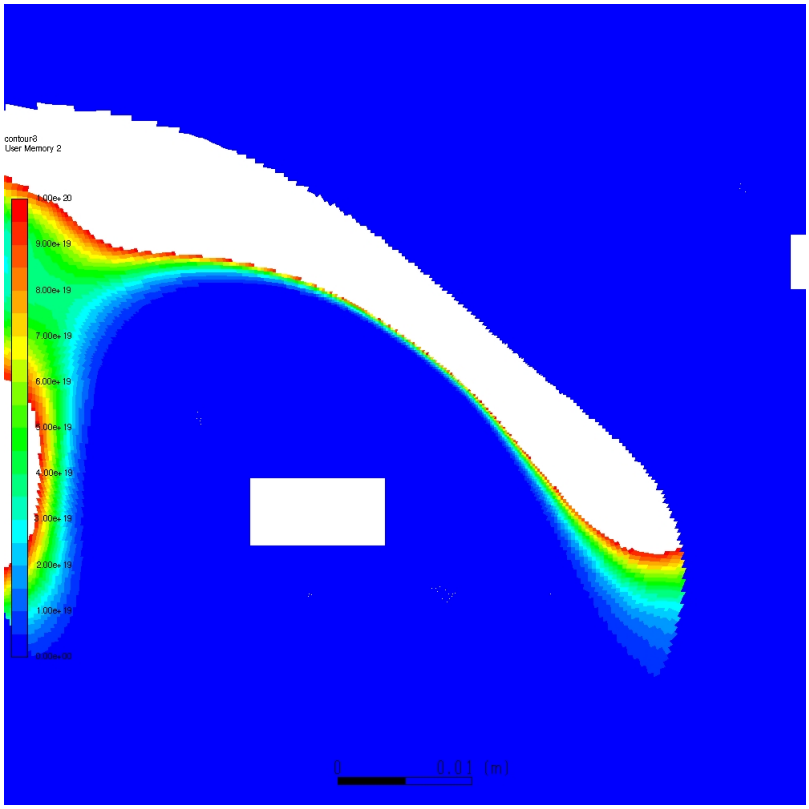

Figure 3.14: Nucleation rate ($m^{-3}s^{-1}$)

Here is represented the nucleation rate as predicted by classical nucleation theory up to 1e20 particles per m^3 per s, where the uncoloured zone depends on the limits of the software to consider numerical values higher than 1e20. We can see the 'nucleation arch' being asymmetrical here, which we can assume to depend on the incoming flux of Argon and all its thermal consequences. We also can make the assumption that most nucleation happens in the uncoloured zone, and specifically the nucleation of very small clusters.

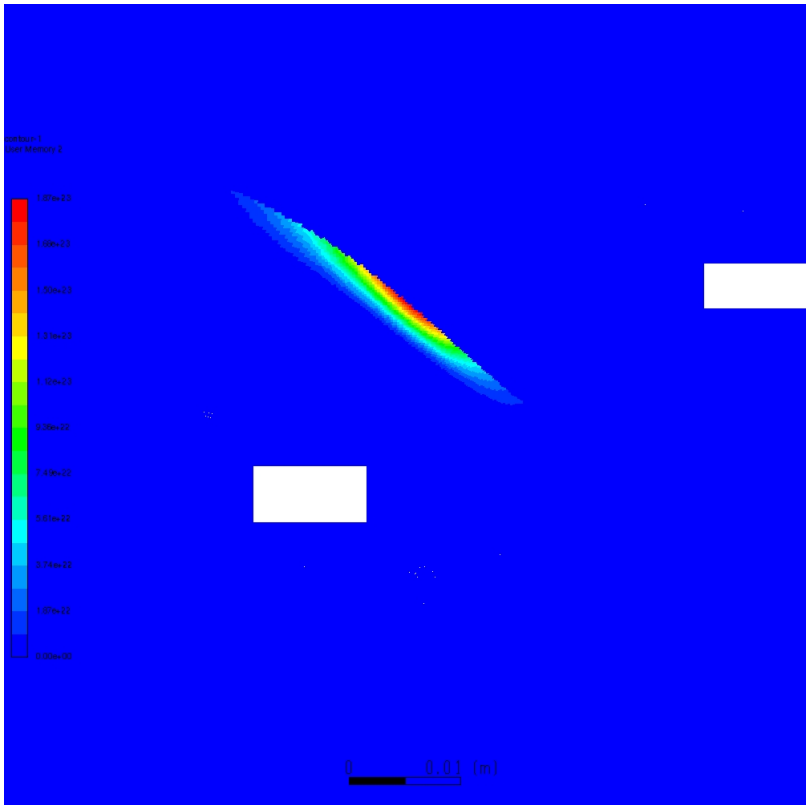

Figure 3.15: Nucleation rate ($m^{-3}s^{-1}$)

In this other image for the nucleation rate we retain the full range of values up to 1.87e23, but without the logarithmic scale. We can see here the existence of a peak of nucleation on the right, which we can assume to be due to the higher temperature gradient visible in fig. 5: something similar to the effect of a fast cooling rate considered in "Homogeneous Nucleation of Particles from the Vapor Phase in Thermal Plasma Synthesis" (S. L. Girshick and C.-P. Chiu, Plasma Chemistry and Plasma Processing, vol.9, n.3, 1989), which we already mentioned in the lines of code.

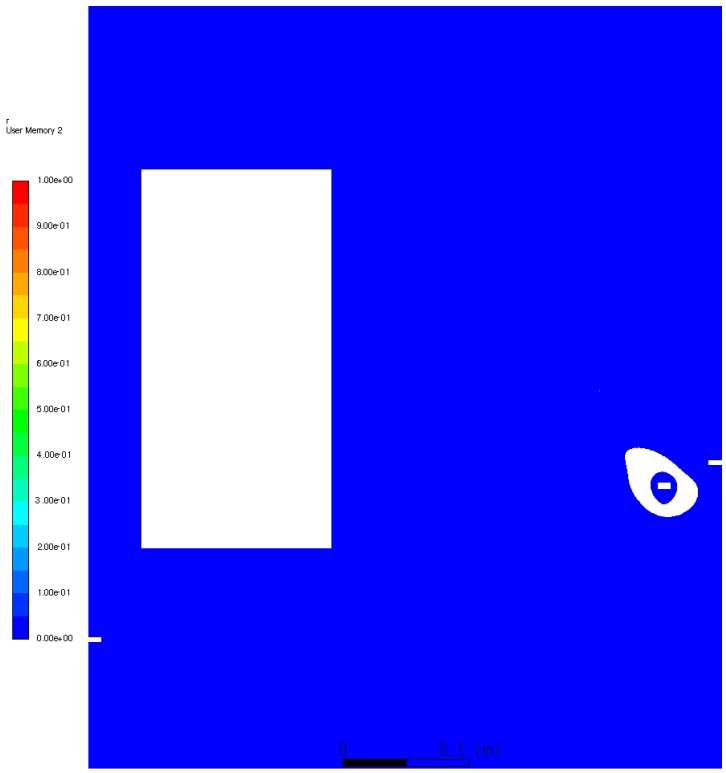

Figure 3.16: Nucleation rate ($m^{-3}s^{-1}$)

Here the nucleation rate is again represented, this time only up to the value of 1 which leaves an uncoloured zone surrounding the crucible, so we can see where nucleation happens in the chamber. An obvious comparison can be done with fig 3.12.

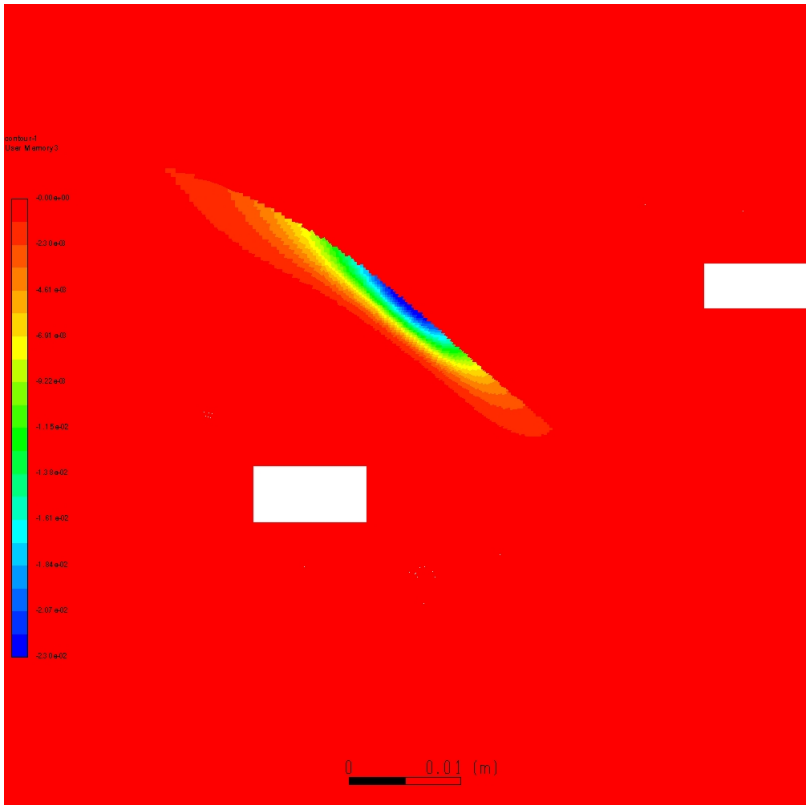

Figure 3.17: Vapour sink (kg/m^3s)

The vapour sink due to nucleation is here given on a non-logarithmic scale going down to -2.3e-2 in correspondence to the peak of nucleation already noted in fig. 3.15, which when confronted with fig. 3.13 explains the low number given for mean particle diameter. We can note though that nucleation ought to occur faster than that in order to add up to the observed generation of nanoparticles in the chamber, which would be of around 10g of powder material (little more than $1cm^3$ of iron) all converted in the timespan of some hours: even assuming that in all the area of fig. 3.16 nucleation occurs at a pace of 2.3e-2 we would still have just some hundreds mg of nanoparticles production per hour, due in particular to the limited area (volume in 3D) where nucleation occurs. This cannot be due to a greater drag of iron vapour in the real chamber, given that there iron monomers disappear with nucleation, cause in any instance, as shown in fig. 3.18, the diminution of monomer concentration is exponential.

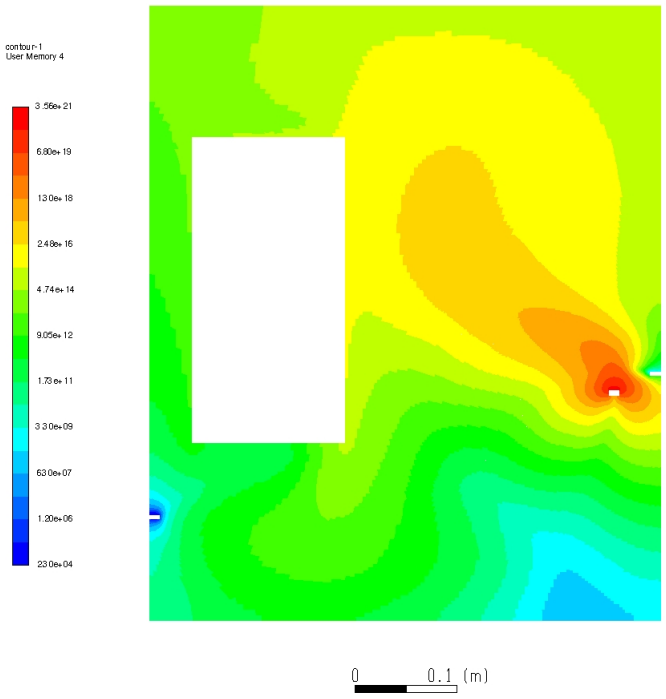

Figure 3.18: Monomer concentration (m^{-3})

Here we see the concentration of iron atoms declining exponentially as distance increases from the crucible, to be compared with the non-logarithmic profile of iron mass fraction in fig. 3.11. We also see here a thermophoretic effect in that iron atoms are dragged toward the cylinder more than toward the outlet in the left part of this figure, while in the right part the effect of the incoming flux is stronger.

3.7 Simulating an Helium atmosphere

A simulation is also run, up to 6000 iterations, switching to an Helium atmosphere: see fig. 3.19 for the residuals, and successive figures for the profiles of velocity and temperature. Just like in the case of Argon atmosphere, confirmations of the validity of the simulation are got by checking density and pressure profile, the latter being uniform as expected while density varies with temperature, and so do viscosity and thermal conductivity which we report here.

The simulation took a certain time to reach a stable pattern like that observed with Argon: this was unexpected since the Rayleigh number (eq. (3.4.3)) of this second

atmosphere turns out to be one order of magnitude inferior to that of the previous case and it was also observed at lower temperature that the Argon atmosphere manifested greater turbulence while an Helium atmosphere resulted in a quasi-laminar flow. This can be explained by the greater momentum of the incoming flux in the previous case which suppressed the convective behaviour.

One important difference with the previous case we observe is that there is more symmetry around the crucible and that the jet coming from inlet is less visible (see e.g. fig. 3.20 and 3.21). A much more symmetrical profile is also seen with nucleation related quantities. The mean particles diameter the program give us is even here around 3.5e-10.

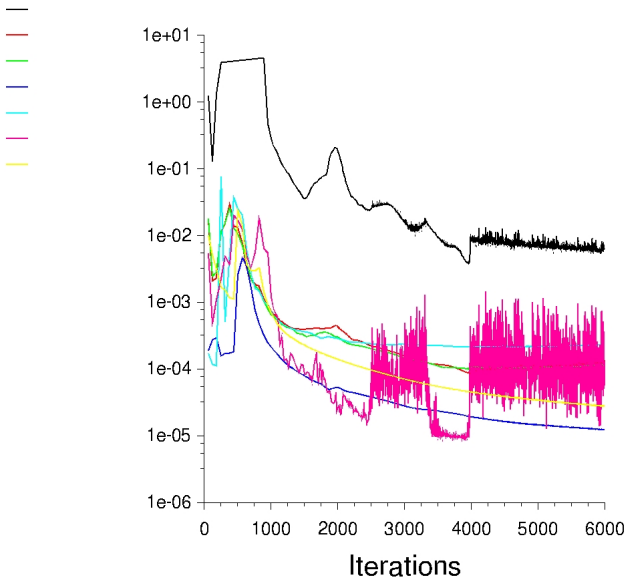

Figure 3.19: Residuals

Here we have the residuals with the same legend we saw in fig. 3.3, and here also the w residual is the more 'difficult' while only the energy residual is really solved according to the chosen convergence criteria. The residuals for x-velocity, y-velocity and continuity also show much less marked oscillations.

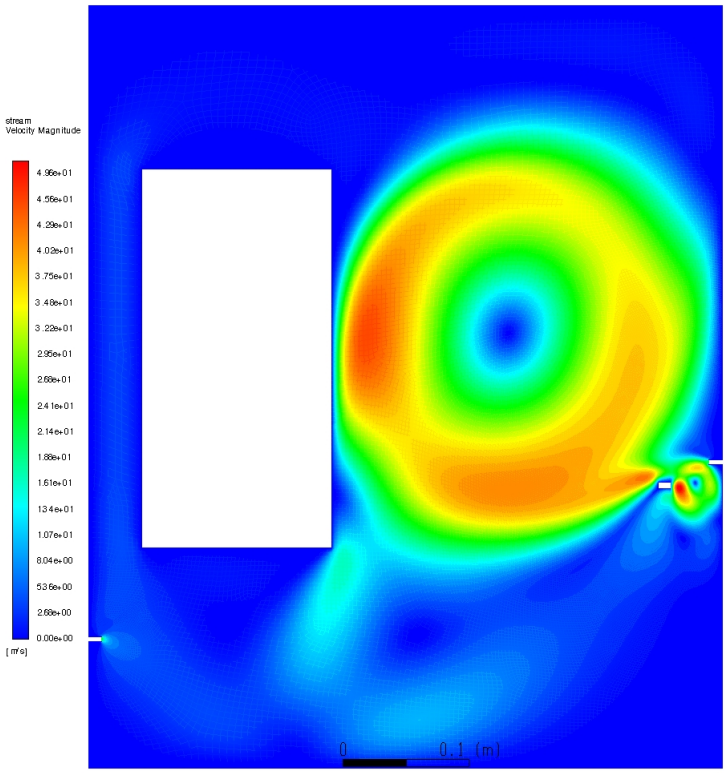

Figure 3.20: Velocity magnitude

Velocity magnitude varies from much more than inlet velocity (49.6 m/s) to almost zero; values under $1.32m/s$ are not registered here, but we can obviously say there is a slow stream from inlet to outlet.

This velocity profile clearly show a convective behaviour lead by the heat coming from the crucible: we can see a variety of circulations, the greater being the one between the right wall and the cylinder, while there also is one near the crucible on the right and a couple under the cylinder.

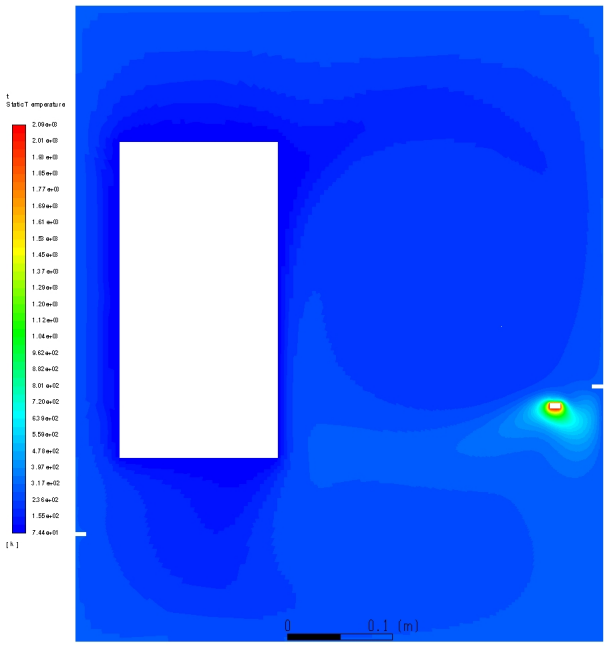

Figure 3.21: Temperature

When compared to fig. 3.5, this profile shows a much less marked effect of the inlet flux on the thermal equilibrium established in the chamber though the profile also show signs of a flux being established between inlet and outlet. Temperature changes from 2100K at the crucible to 300K at the walls and 70K on the cylinder, the rapid change on the left of the crucible being due to the high thermal conductivity of helium and the energy being dragged in the convective movement that is established.

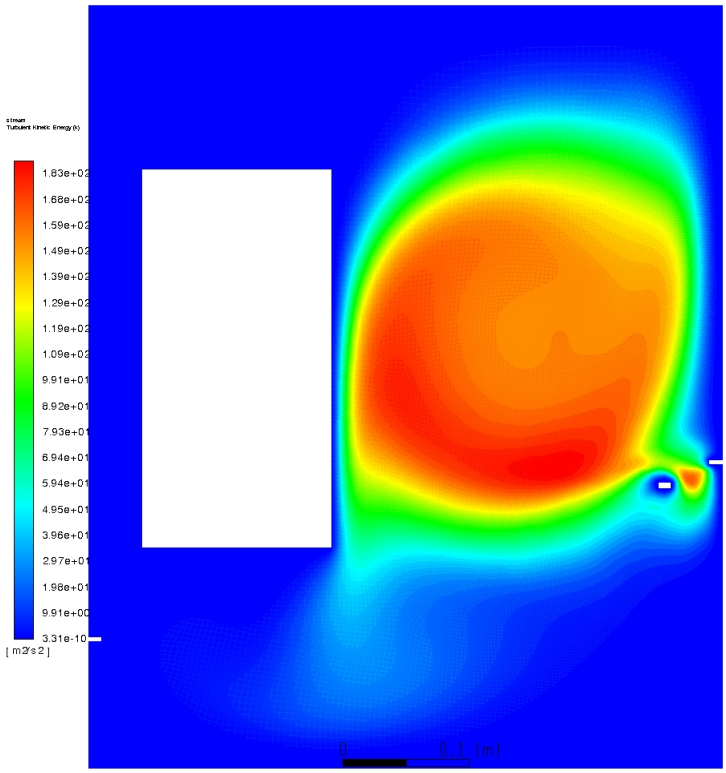

Figure 3.22: Turbulent kinetic energy

Turbulence kinetic energy is represented on a non-logarithmic scale from near zero to 1.83e2 m^2/s^2. The profile observed is in good agreement with the velocity profile and when compared with fig. 3.6 shows a much more significant turbulent behaviour.

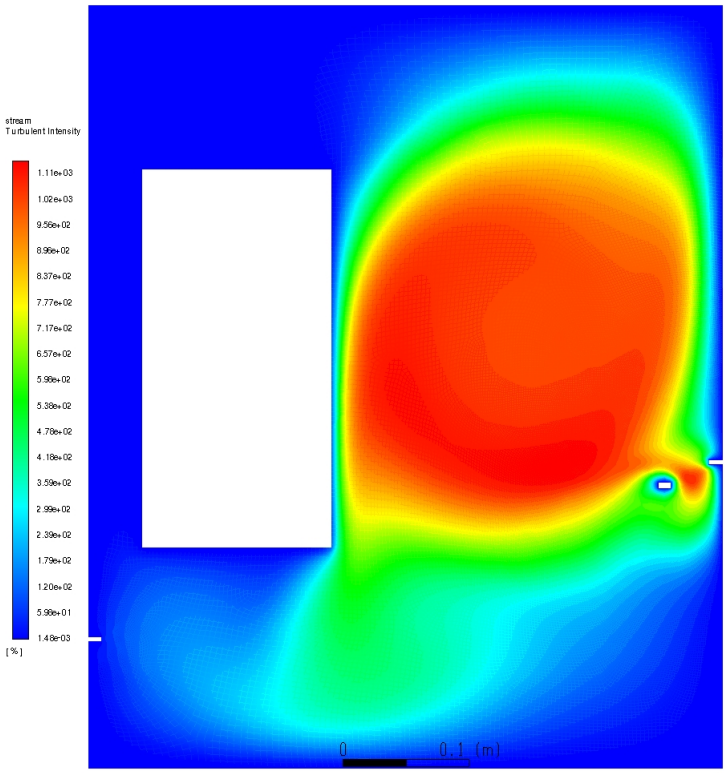

Figure 3.23: Turbulence intensity

Turbulence intensity ranges here up to 1.11e3%, and shows the same profile already seen for turbulent kinetic energy. The comparison with fig. 3.7 highlights the much more turbulent nature of this atmosphere.

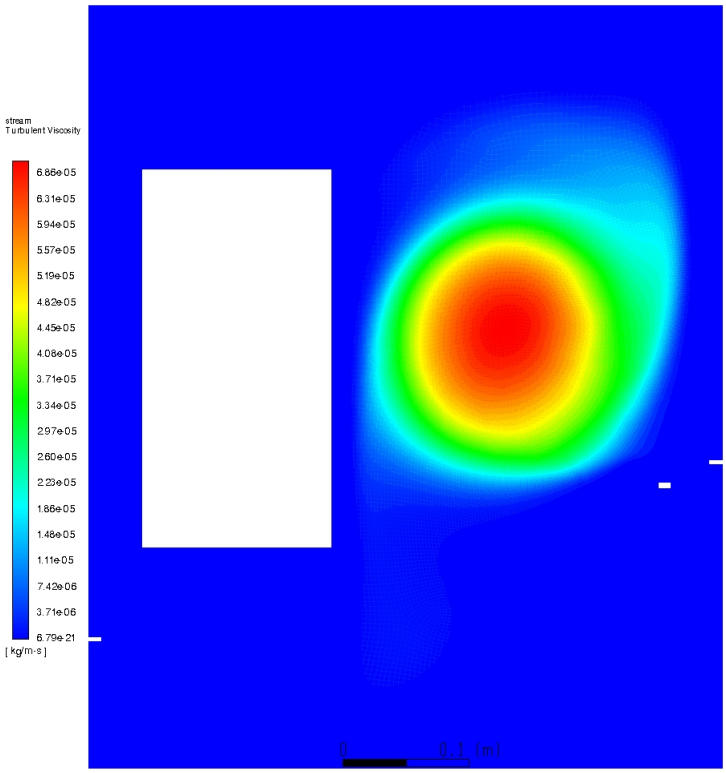

Figure 3.24: Turbulent viscosity

Turbulent viscosity arrives here at a maximum of 6.86e-5 (MKS units) which is much more than what we saw in fig. 3.8: here the part of apparent viscosity due to turbulence is clearly higher, in the centre of the chamber, than that due to Helium properties, which (see eq. (3.4.10)) is due primary to the great amount of turbulent kinetic energy already observed in fig. 3.22. This profile here is clearly located where the convective motion happens, while in fig. 3.8 turbulent viscosity was located lower in the chamber.

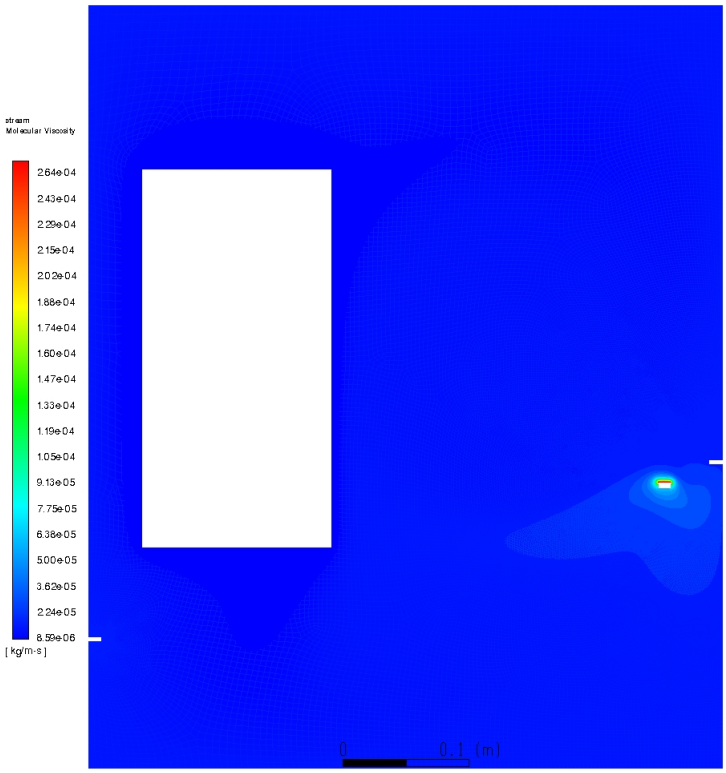

Figure 3.25: Molecular viscosity

Molecular viscosity varies in the range between 8.59e-6 and 2.64e-4 (MKS units), and in agreement with the temperature profile there are no big changes outside the zone immediately near the crucible; the values found are perfectly in line with what the literature suggests for Helium properties, iron being meaningfully present only near the crucible. Difference and similarities with the profile in fig. 3.9 are understandable in term of the temperature profiles of the two cases respectively: here we don't see the jet of incoming gas.

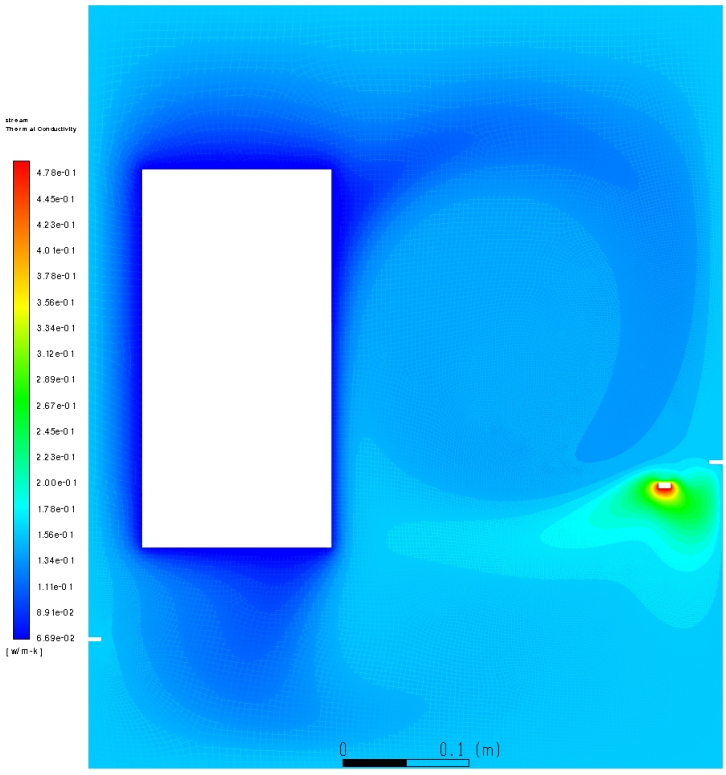

Figure 3.26: Thermal conductivity

Much like with fig. 3.25 and fig. 3.21, here we have the profile of thermal conductivity ranging between 6.69e-2 and 4.78e-1 (MKS units), in agreement with what expected from documented Helium properties. The imagine here also makes the presence of convection much clearer due to the less wide range of values than in fig. 3.25.

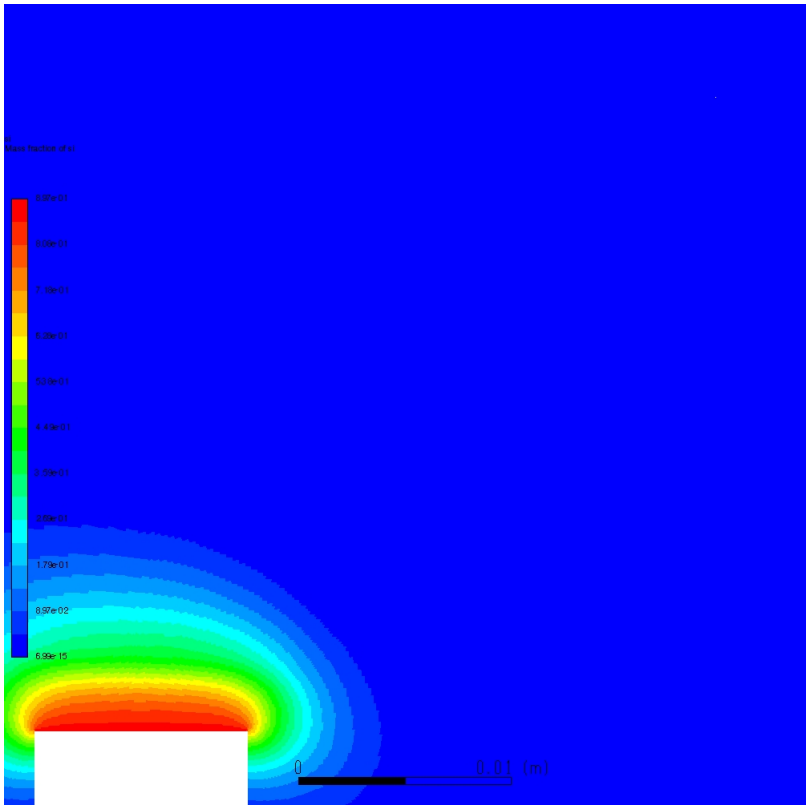

Figure 3.27: Composition: mass fraction of iron

This profile of composition is very similar to that of fig. 3.11, except of course that the mass fraction of iron vapour immediately near the crucible's wall is here put at 96%, which specifically depends on helium atoms being less massive. Just like in the previous case, one has to consider a logarithmic profile to get a wider idea of the diffusion of iron atoms in the chamber (see fig. 3.32 for monomer concentration).

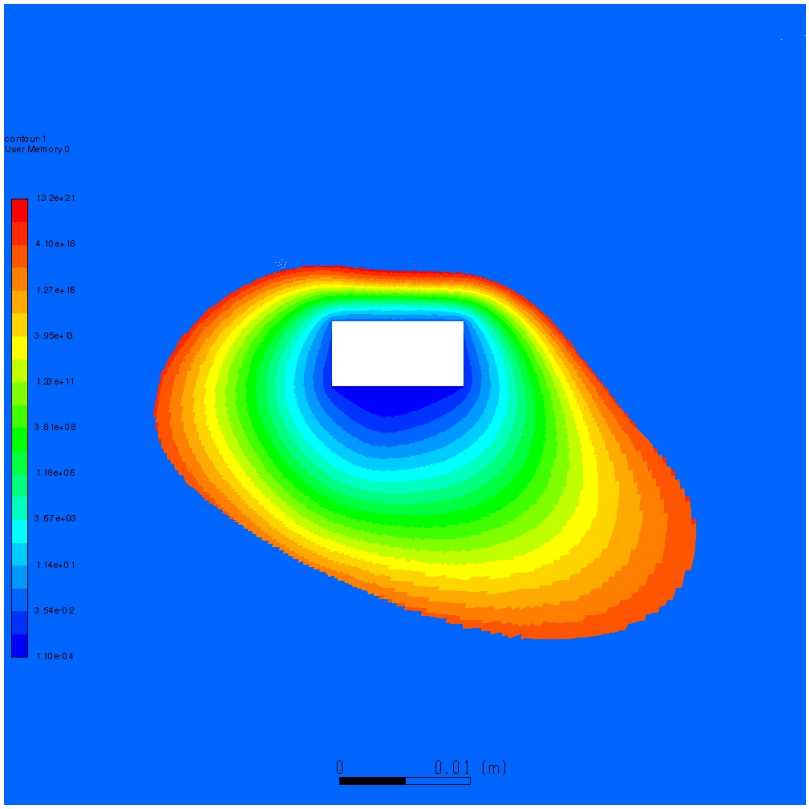

Figure 3.28: Saturation ratio

The profile of saturation ratio in an helium atmosphere, when compared to fig. 3.12, shows a more symmetric course over the crucible and a prolongation on the right under the inlet which is due to a small jet in that zone visible in the velocity and temperature profile. In this case its value goes up to 1.32e21 in the supersaturation zone, but, since in determining both the critical volume and the nucleation rate the logarithm of it is what counts, this doesn't amount to a great difference with the 8.07e19 seen in the previous case.

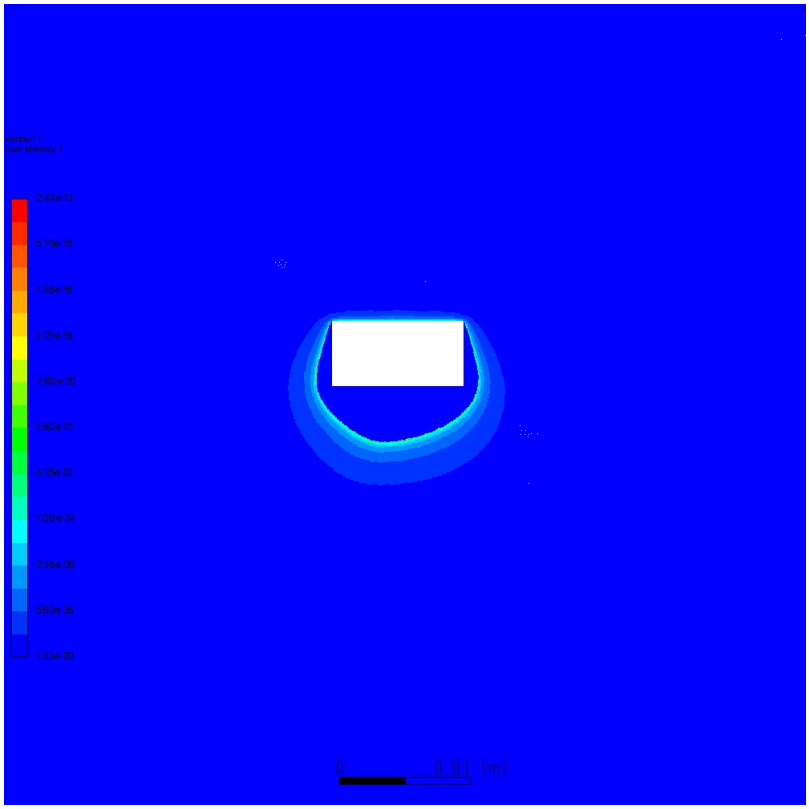

Figure 3.29: Critical volume (m^3)

Here we have, up to the value of 2.43e-13, the minimal critical volume for stable nanoparticles formation, the profile being different in shape to that seen in fig. 3.13 because of the greater maximum value attained very near to the crucible; this can be considered of secondary importance given the low nucleation rate in that zone, in agreement with the very similar mean particle diameter computed in the two cases.

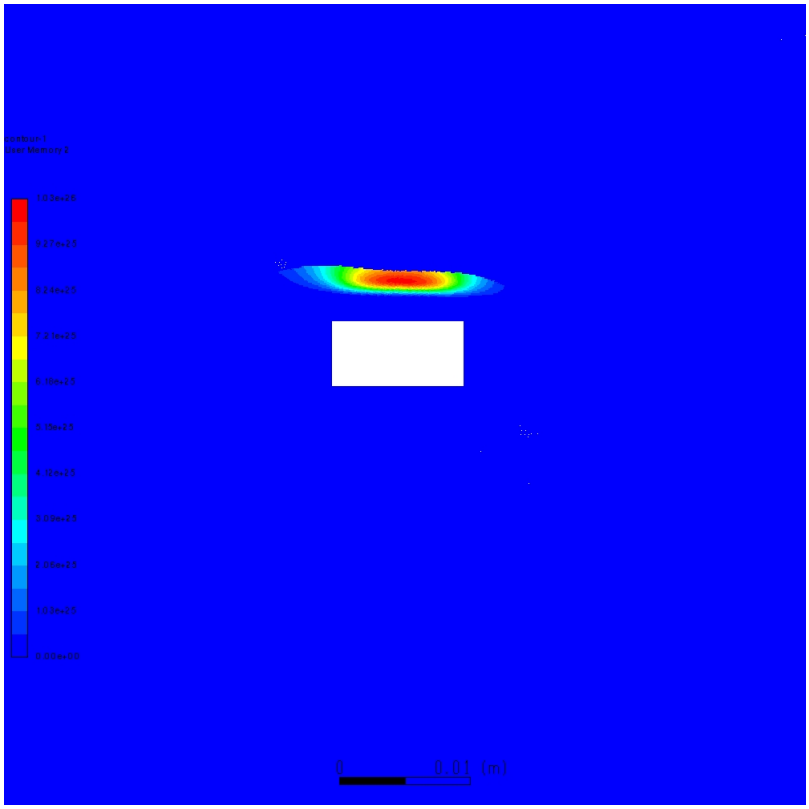

Figure 3.30: Nucleation rate ($m^{-3}s^{-1}$)

We see here the nucleation 'arch' over the crucible which obviously differs from that seen in fig. 3.14 and 3.15 for its symmetry, as we also saw for the temperature profile: the relative uniformity of the temperature gradient is indeed the most reasonable explanation of such change. There also is a difference in the quantity of nucleation episodes computed (each s per m^3): here we have at most 1.05e26 which is one order of magnitude higher that what has been computed for an Argon atmosphere: that also is related to the temperature gradient which, as one can see comparing fig. 3.5 and 3.21, is greater for an Helium atmosphere, mainly because of the higher thermal conductivity.

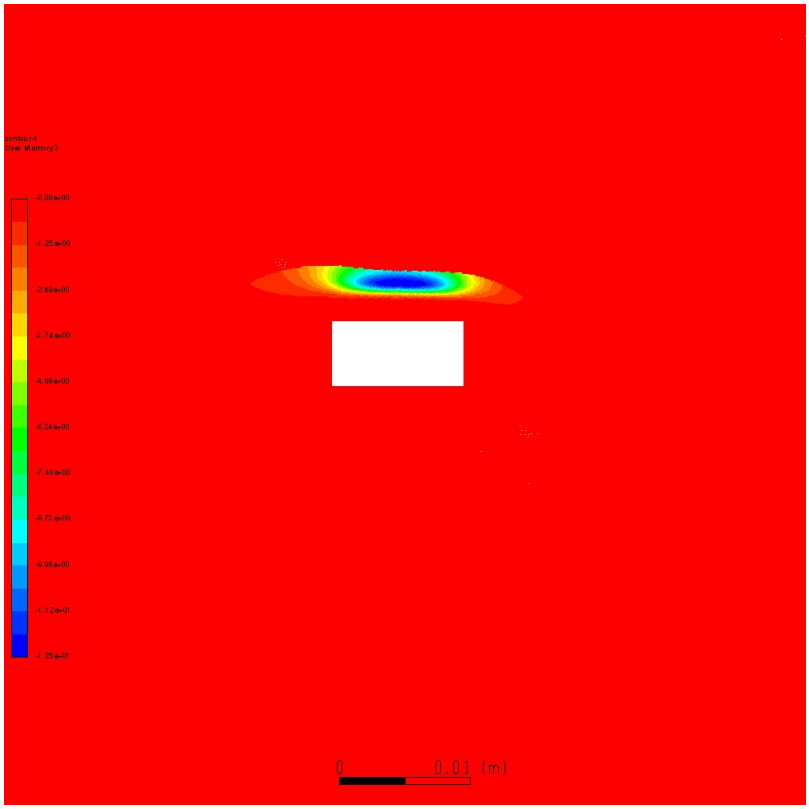

Figure 3.31: Vapour sink (kg/m^3s^1)

Vapour sink is here represented on a linear scale down to -1.25e1, the resulting profile being the same as that of fig. 3.30 as one would expect: looking at fig. 3.29 one can see that the volume of nucleated particles decreases very much going from the crucible to the 'arch', which leaves the number of nucleation events as the only factor determining the vapour sink. In a comparison with fig. 3.17, other than the much greater symmetry of this profile, we can observe that the vapour sink is here three orders of magnitude greater, as already seen for the nucleation rate, eliminating entirely the problem of insufficient nanoparticles production.

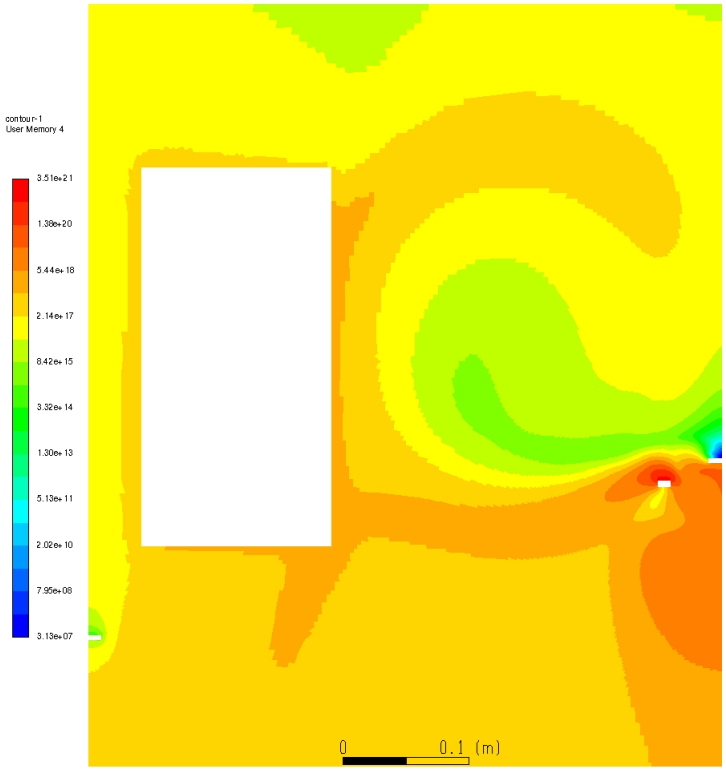

Figure 3.32: Monomer concentration (m^{-3})

Since the difference in the given mass fraction of iron is due to the different atomic weight of Helium and Argon, the quantity of monomers per unit volume being similar to that seen in fig. 3.18 is expected. The differences with the profile of fig. 18 are readily comprehensible based on both the presence of a convective motion and the absence of a strong horizontal jet, as already observed when comparing the velocity profiles.

3.8 Some conclusions

As seen in fig. 3.18 and 3.32, which only account for single atoms, thermophoresis (included in the Fluent model for species diffusion) does indeed influence the movement of particles from the crucible to the cylinder. While for Knudsen number approaching unity (free molecules range) the thermophoretic drag velocity which is independent on particle properties, but since we are in the continuum regime (eq. 1) we write (see

'Smoke, Dust and Haze', Sheldon K Friedlander):

$$v_{th} = \frac{2C_s\eta\frac{k_g}{k_p}\frac{\nabla T}{T}}{1+2\frac{k_g}{k_p}} \tag{3.8.1}$$

where C_s is a coefficient that can be computed from kinetic theory and that is general assumed to be around 1.14 for complete thermal accommodation, while k_g and k_p are respectively the thermal conductivity of the gas and the nanoparticles. We already know the thermal conductivity of Argon and Helium to be always below 7.60e-2 and 4.55e-1 respectively (MKS units), while nanoparticles conductivity we assume to be not below 1.39 (MKS units) based on what can be found in literature (see e.g. 'Size-dependent thermal conductivity of nanoscale semiconducting systems', L. H. Liang and Baowen Li,Phys. Rev. B 73, 153303, 2006)

Considering that the temperature declines from 2100 K to 70 K going from the crucible to the cylinder we will average the temperature gradient to be around 60 K/cm. Averaging temperature at 300 K and taking the value of 2.15e-5 (MKS units) for viscosity (no great difference between the two atmospheres), we would have based on eq. (3.8.1) v_{th} to be only around 1e-5 m/s. We will thereby assume that the thermophoretic drag directly between the crucible and the cylinder cannot be the driving force governing the motion of nucleated particles, which then will adhere to the cylinder once arrived near there.

In order to study the growth of nanoparticles due to condensation and coagulation we take a streamline computed based on the chamber hydrodynamic characterization (see fig. 3.33 and 3.34, taken with the software ParaView).

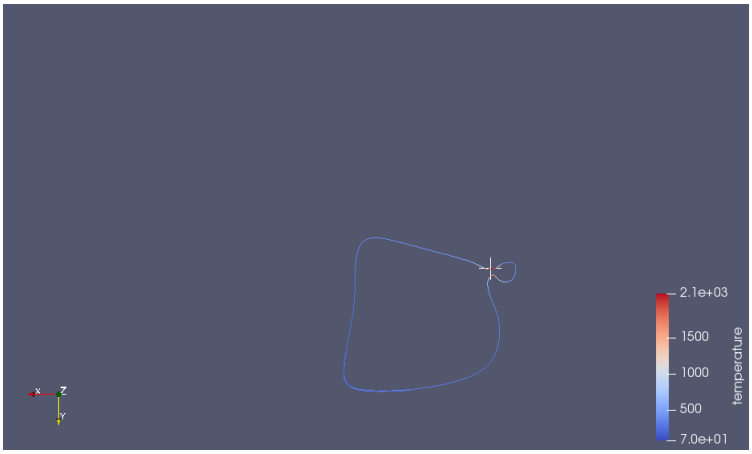

Figure 3.33: Streamline(Ar)

The streamline is taken starting from near the crucible where nucleation is supposed to happen: we also have in a separate file the various data of pressure (basically uniform)

and, most important, temperature associated with the time at which the particle occupies a given position

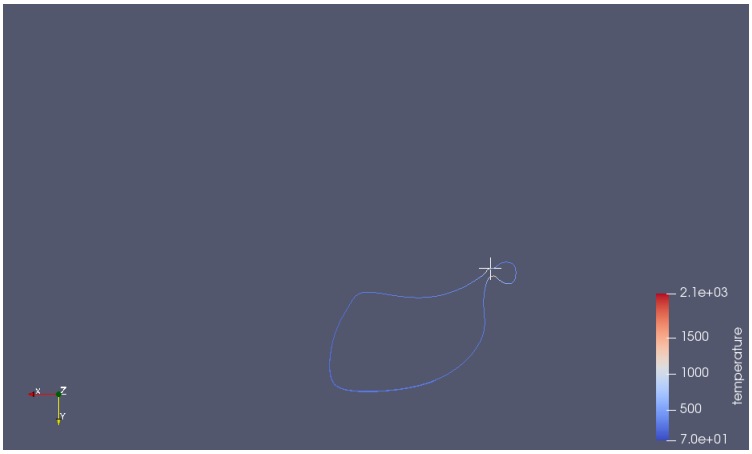

Figure 3.34: Streamline(He)

The similarities between the streamlines would seem to indicate a little influence of the different atmospheres in the process of nucleation, which would not depend on convective flux for its results.

3.9 Data analysis and experimental comparison

We take the data of the streamlines organized in files with temperatures associated to any given time from the origin of the flux, taken near the crucible. We process those data in order to obtain the growth of the nucleated particles as a result, due in particular to the processes of condensation and coagulation.

After a failed attempt to directly implement the moment equations (see "Smoke, Dust and Haze", Sheldon K Friedlander) in the fluent simulations, which resulted in amplifying errors and not giving a stable solution for the growth of nanoparticles, we turned to the Pratsinis Model as a way to simulate growth of nanoparticles along the streamlines extracted from the simulations. Characteristics of the Pratsinis Model are the assumption of a lognormal distribution and the possibility to model both growth by condensation and coagulation by collisions (see The Nanodome Project symposium, March 21-22, 2017, NETZ, University Duisburg-Essen, Duisburg, Germany: here one can also find a comparison with the Friedlander Model). The key to the functioning of all moments methods is in any case given by the use of separate variables for different powers of particles volume that can be made to evolve according to the relevant equations.

Here we have the lines of code of the cnt.cpp used to apply classical nucleation theory to get nanoparticles' formation, where we can see the presence of a term for the

condensation together with the nucleation part that repeats what already done in the fluent simulations.

```
/*
    NanoDome - H2020 European Project NanoDome, GA n.646121
    (www.nanodome.eu, https://github.com/nanodome/nanodome)
    e-mail: Emanuele Ghedini, emanuele.ghedini@unibo.it

    Copyright (C) 2018  Alma Mater Studiorum - Università di Bologna

    This program is free software: you can redistribute it and/or modify
    it under the terms of the GNU Lesser General Public License as
    published by the Free Software Foundation, either version 3 of the
    License, or (at your option) any later version.

    This program is distributed in the hope that it will be useful,
    but WITHOUT ANY WARRANTY; without even the implied warranty of
    MERCHANTABILITY or FITNESS FOR A PARTICULAR PURPOSE.  See the
    GNU General Public License for more details.

    You should have received a copy of the GNU General Public License
    along with this program.  If not, see <http://www.gnu.org/licenses/>.
*/

#include "cnt.h"

#include <cmath>
#include <limits>
#include <exception>
#include <stdexcept>
#include <iostream>

ClassicalNucleationTheory::ClassicalNucleationTheory(Species _species) :
    species(_species) { }


double ClassicalNucleationTheory::nucleation_rate(double T, double S)  const {

    double rate = 0.0;
//unsigned int fp_control_state = _controlfp(_EM_INEXACT, _MCW_EM);
```

```
    // check if species is saturated, if not nucleation rate is left to zero
    if(S>1.0) {

        // normalized surface tension
        double theta = species.s_ten(T)*species.m_surface()/(K_BOL*T);
        double ns_sat = species.n_sat(T);

        double A = (S*ns_sat*ns_sat);
        double B = species.m_volume();
        double C1 = 2.0*species.s_ten(T);
        double C2 = M_PI*species.get_mass();
        double D1 = theta - 4.0*pow(theta, 3) / (27.0*pow(log(S), 2));
        double C = sqrt(C1 / C2);

double D = exp(D1);

rate = A * B * C * D;

    } else if (S==1) {

        rate = std::numeric_limits<double>::min();
    }

    return rate;
}


double ClassicalNucleationTheory::stable_cluster_size(double T, double S) const {

    double c_size = 1.0;

    // check if species is saturated; if not, the stable size has no sense and is set
    // meaning that the smallest cluster is a single monomer (no-cluster)
    if(S>1) {
        c_size = 2.0 * species.m_surface() * species.s_ten(T) / (3*K_BOL*T*log(S));
        c_size = pow(c_size,3);
}

    return c_size;
}
```

```
double ClassicalNucleationTheory::stable_cluster_diameter(double T, double S) const {

    return 2*pow( (3./4.) * species.m_volume() * stable_cluster_size(T,S) / M_PI, 1./
}


double ClassicalNucleationTheory::condensation_rate(double T, double S) const {

    return species.p_sat(T)*(S-1.0) / sqrt(2*M_PI*species.get_mass()*K_BOL*T);
}
```

We also show some of the Pratsinis Model lines of code (momentodelpratsinis.cpp) that introduce the moments and deal more specifically with growth by condensation and coagulation.

```
    // temporary moments values
    double M0_, M1_, M2_;

    // volume of the critical size cluster
    // if S<1 the NucleationTheory object should return 1 as stable critical cluster
    double vm = j * species.m_volume();

/// dissipation limit
double vm1 = 0.0;


     // nucleation source for each moment
    double M0_nucl = J;
    double M1_nucl = J * vm;
    double M2_nucl = J * vm*vm;

    double vg = geometric_mean_v();
    double ln2sg = ln2_standard_dev();

    // condensation source for each moment
//double M1_cond;
double M2_cond;
M1_cond = csi1(T)*(S - 1)*M_k(2. / 3., ln2sg, vg);
M2_cond = 2 * csi1(T)*(S - 1)*M_k(5. / 3., ln2sg, vg);
```

```
// coagulation source for each moment
  double M0_coag =   csi2(T)*zeta0(sg)*(  M_k(2./3.,ln2sg,vg) * M_k(-1./2.,ln2sg,vg
                                        2*M_k(1./3.,ln2sg,vg) * M_k(-1./6.,ln2sg,vg
                                          M_k(1./6.,ln2sg,vg) * M0);

  double M2_coag = 2*csi2(T)*zeta2(sg)*(  M_k(5./3.,ln2sg,vg) * M_k(1./2.,ln2sg,vg)
                                        2*M_k(4./3.,ln2sg,vg) * M_k(5./6.,ln2sg,vg)
                                          M_k(7./6.,ln2sg,vg) * M1);


  // moments equations solution (simple first order explicit method) (TO BE IMPROVE
  M0_ = M0 + (M0_nucl           - M0_coag - M0_diss) * dt - gamma*M0*dt;
  M1_ = M1 + (M1_nucl + M1_cond           - M1_diss) * dt - gamma*M1*dt;
  M2_ = M2 + (M2_nucl + M2_cond + M2_coag - M2_diss) * dt - gamma*M2*dt;
```

where we also see the presence of dissipative terms that account for the evaporation of particles.

When the streamlines taken from fluent are used with this program the result is that nanoparticles are expected to grow up to 4.09 nm in an Argon atmosphere and 0.29 nm in an Helium atmosphere which contradicts the experimental findings of an order of magnitude in both cases: observed values are of the order of 5 to 15 nm in an Helium atmosphere and up to 50 nm in an Argon atmosphere.

The fact that nanoparticles end up being much bigger in an Argon atmosphere is indeed exactly what we observe, and the difference in size is approximately of this order, but the failing of the simulation to give the expected final values cannot be explained by some marginal factor of the simulation, the temperature being already higher of a couple hundreds kelvin than the iron melting point. Moreover, while this is not exactly true for the Argon case, we see in fig. 3.31 that at least with Helium the nanoparticles production rate is realistically high enough. This is unexpected given that the parallel work of Giorgio La Civita on silver nanoparticles has shown a good agreement between experimental data and what observed; however, in that case the Population Balance Method (PBM: see again The Nanodome Project symposium) was applied which is known to give better results in a variety of situations.

The Friedlander Model also has been applied to the same streamlines, giving however a similar result, in agreement with the compatibility of the two approaches shown elsewhere in literature. In order to test whether it is possible to arrive to a better result two other possible streamlines, which describe the convective motion over the crucible, were considered (see fig. 3.35 and followings) but with no improvement.

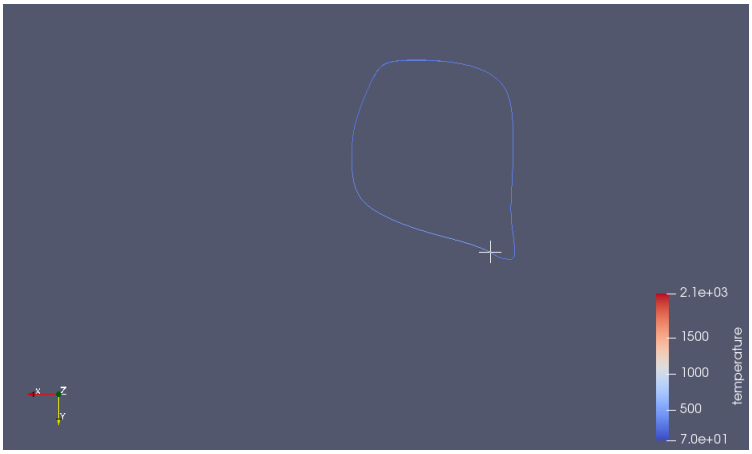

Figure 3.35: Streamline1(Ar)

This streamline from the Argon case has given a worse result when either the Pratsinis Model or the Friedlander Model is applied: 0.30nm. This clearly confirms that the growth of nanoparticles does not occur far from the crucible.

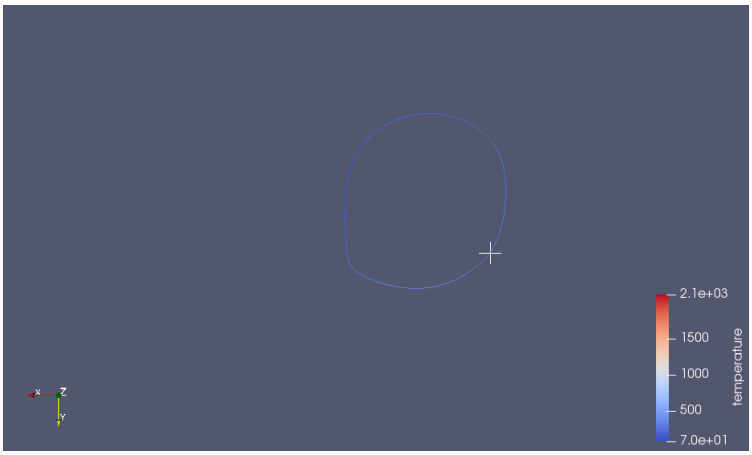

Figure 3.36: Streamline1(He)

This streamline from the Helium case also did give no improvement in terms of final nanoparticles dimensions: we get 0.29nm with both the Pratsinis and Friedlander Model.

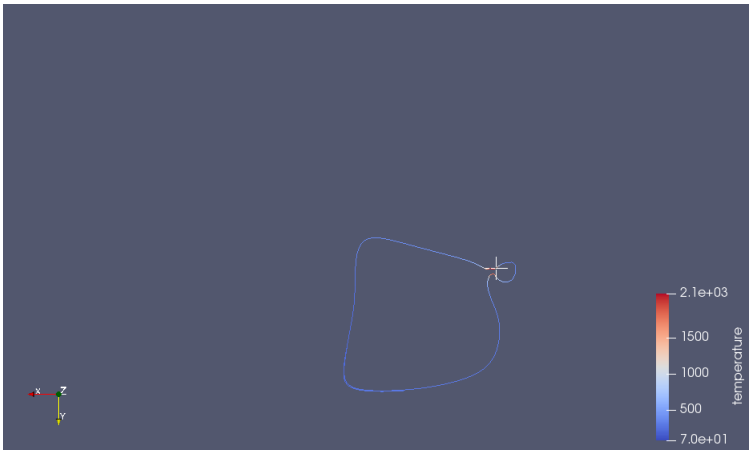

Figure 3.37: Streamline2(Ar)

In this case we tried to take more into account high temperatures nearer the crucible, but we still get only about 2.9nm.

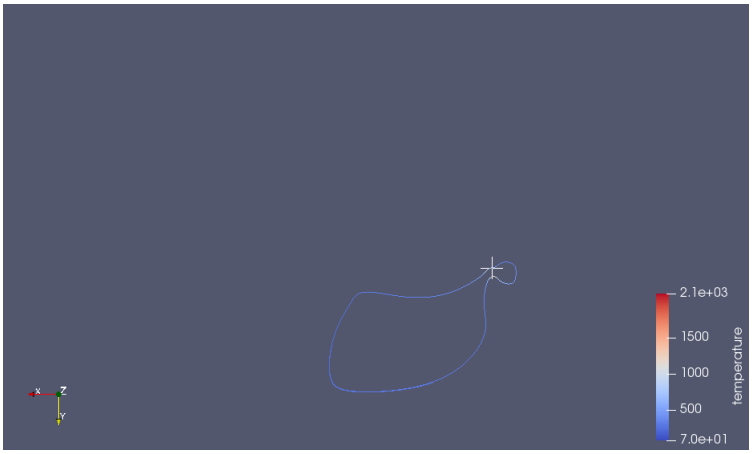

Figure 3.38: Streamline2(He)

Trying to bring the streamline origin nearer the crucible doesn't change the result, which still consists of clusters of few atoms.

3.10 Conclusions

We were able to characterize hydrodynamically the chamber and establish the place where nucleation occurs, just above the crucible, while the process of growth of these nanoparticles remains elusive, particularly for an Helium atmosphere, though we can

exclude nanoparticles growth occurring at a great distance from the crucible; higher thermal conductivity is the cause of the smaller dimension of nanoparticles produced with an Helium atmosphere, while turbulence would seem to play a less relevant role. Further research, apart from the application of PBM, should improve the precision in simulating near-crucible behaviour. We were able to verify the similarity of the results obtained with the Pratsinis and Friedlander approaches.

REFERENCES

Kinetics of Materials, Robert W. Balluffi, Samuel M. Allen, Craig W. Carter, published by: Hoboken, N.J. : J. Wiley Sons, 2005

Dust, Smoke and Haze, Sheldon K Friedlander, published by: New York • Oxford OXFORD UNIVERSITY PRESS 2000

Patelli, N.; Migliori, A.; Morandi, V.; Pasquini, L. One-Step Synthesis of Metal/Oxide Nanocomposites by Gas Phase Condensation. Nanomaterials 2019, 9, 219.

OhSK Modified Lennard–Jones potentials with a reduced temperature-correction parameter for calculating thermodynamic and transport properties: noble gases and their mixtures (He, Ne, Ar, Kr, and Xe) J. Thermodyn. 2013 828620

Metal vapour pressure table mmrc.caltech.edu

ANSYS Manual, 2012, ANSYS–FLUENT 12.0, Theory Guide

Surface tension of nickel, copper, iron and their binary alloys (JOURNAL OF MATERIALS SCIENCE 40 (2005) 2213– 2216, J. BRILLO, I. EGRY)

"Homogeneous Nucleation of Particles from the Vapor Phase in Thermal Plasma Synthesis" (S. L. Girshick and C.-P. Chiu, Plasma Chemistry and Plasma Processing, vol.9, n.3, 1989)

Size-dependent thermal conductivity of nanoscale semiconducting systems, L. H. Liang and Baowen Li,Phys. Rev. B 73, 153303, 2006

The Nanodome Project symposium, March 21-22, 2017, NETZ, University Duisburg-Essen, Duisburg